

Multi-Method Fault Detection of Cooling Fan in Control Cabinet using Temperature Analysis

Michael Keenan Odena, Lasse Bonde Hansen

Offshore Energy Systems, OES4-4,
Spring Semester 2023

Master Thesis





Energy Technology
Aalborg University
<https://www.aau.dk>

AALBORG UNIVERSITY

STUDENT REPORT

Title:

Multi-Method Fault Detection of Cooling Fan in Control Cabinet using Temperature Analysis

Theme:

Master Thesis

Project Period:

Spring Semester 2023

Project Group:

OES4-4

Participants:

Michael Keenan Odena
Lasse Bonde Hansen

Supervisors:

Zhenyu Yang
Frank Vandborg (Siemens Gamesa)

Page Numbers: 69

Date of Completion:

31st May 2023

Abstract:

This report details the development of diverse fault detection and diagnosis algorithms employed for detecting faults in cooling fans utilized for temperature management in control cabinets of wind turbines. To replicate the thermodynamic behavior of an actual cabinet, two models were created: a single-zone model and a multi-zone model. These models simulated and collected temperature measurements of both the cabinet and the nacelle. To identify the system parameters, a calibration phase utilizing the Recursive Least Squares (RLS) method was implemented based on the temperature measurements. The acquired parameters, along with the measurements, were then employed in the fault detection and diagnosis (FDD) algorithms, including a bank of Observers, Multiple Model Adaptive Estimation (MMAE), and Joint State estimation. Through these methods, reliable temperature estimation and prediction of the cooling fans' health status within a certain range were achieved.

Contents

Preface	1
1 Introduction	2
1.1 Control Cabinets	4
2 Problem Analysis	5
2.1 State of the art	5
2.2 Summary	7
3 Task Statement	8
3.1 Task Statement	8
3.2 Delimitation	8
4 Modelling	9
4.1 Setup	9
4.2 Single-zone Model	11
4.2.1 Thermal Dynamics	11
4.2.2 Simulation	13
4.3 Multi-zone model	15
4.3.1 Thermal Dynamics	15
4.3.2 Simulation	19
5 Methodology	23
5.1 Parameter Estimation	23
5.1.1 Least Squares Method	23
5.1.2 Recursive Least Squares (RLS)	24
5.1.3 Forgetting Factor Recursive Least Squares (FFRLS)	25
5.2 State Estimation	25
5.2.1 State Observer	26
5.2.2 Kalman Filter	26
5.2.3 Extended Kalman Filter	27

6	Results	28
6.1	Calibration	28
6.2	Modelling fault in fans	34
6.3	Bank of Observers	35
6.3.1	Pole placement	36
6.3.2	Observer Design	36
6.3.3	Simulation with fault	37
6.3.4	Observer Test	38
6.3.5	Results	41
6.4	Multiple Model Adaptive Estimation (MMAE)	43
6.4.1	Test	44
6.4.2	Results	45
6.4.3	Likelihood function	47
6.5	Joint state estimation	50
6.5.1	Observability	51
6.5.2	Results	51
6.6	Validation	53
6.6.1	Fault scenarios	53
6.6.2	Calibration	55
6.6.3	Bank of Observers	57
6.6.4	MMAE	59
6.6.5	Joint State Estimation	60
7	Discussion	62
8	Conclusions	64
	Bibliography	66

Preface

This Master's Thesis was created by Master's students of Offshore Energy Systems at Aalborg University Esbjerg, and was written during the spring semester of 2023. The group thanks Zhenyu Yang for supervising this project and Frank Vandborg from Siemens Gamesa for proposing the topic.

Aalborg University, 31st May 2023



Michael Joseph Keenan Odena
<mkeena21@student.aau.dk>



Lasse Bonde Hansen
<lh18@student.aau.dk>

Chapter 1

Introduction

Energy demand has been increasing over the last decades around the world, and fossil fuels have been the leading source, providing around 80% of the total energy demand. This has caused greenhouse emission gases to negatively impact the climate. For that reason, agreements such as the one established in Paris (2015), aim to limit global warming to 2°C above the pre-industrial levels [1]. However, according to the World Energy Outlook 2022 (IEA), this trend is finally switching with the prediction of declining (currently at around 70% of fossil global demand) and being replaced by the growing scope of renewable energies [2].

It can be observed from the below Figure 1.1 how the prediction for the future of global energy are dominated by the decline of hydrocarbons, the rapid expansion of renewable energy sources, and the increase of electrification and the use of low-carbon hydrogen.

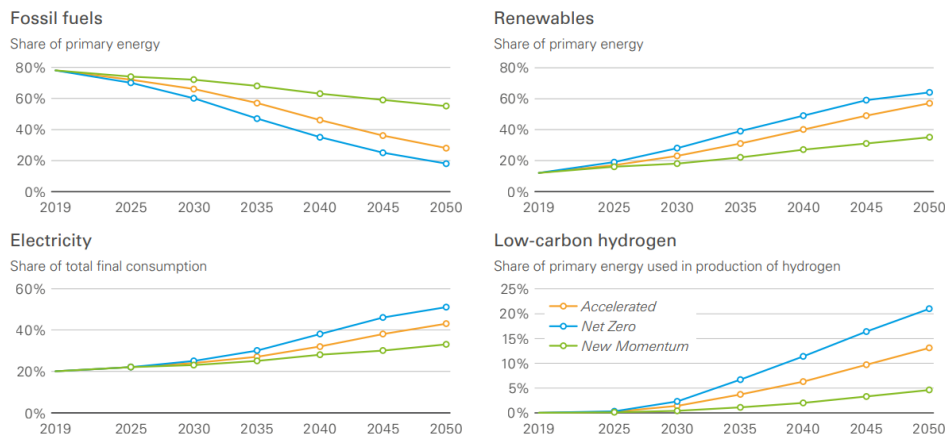


Figure 1.1: Global energy prediction by energy source [3]

The emission of greenhouse gases has negatively impacted the climate, therefore,

to prevent a higher growth in the average global temperature and speed up the green transition to a low-carbon scene, the implementation of emission-free power sources is required, such as wind. Wind power is a renewable energy technology that harnesses the kinetic energy from the movement of the wind and converts it into mechanical energy and electricity, without consuming fuels or producing carbon emissions. Currently, most wind energy develops from turbines. The kinetic energy created by the air in motion provides the initial force to turn the blades on the turbine that, through a shaft connected to a generator, provides the mechanical energy to produce electricity.

In the last few decades, both the physical dimensions and power-generating capability of wind turbines have increased due to the huge market demand and technological advances [4, 5]. Wind turbines are becoming complex machines that operate under harsh conditions and, over time, will decline in performance and efficiency. This situation has led to focus on maintenance and fault detection topics. Although technology has improved to minimize failure rates, wind turbine failures are constantly occurring. Major faults, such as the gearbox, generator, yaw system, or rotor, represent 25% of all failures but account for 95% of the downtime [6]. These failures often result in an extended downtime lasting more than a day, require costly repairs, and inhibit power generation [7]. Also, wind farms have been rapidly expanding in recent years and are located in onshore and offshore remote sites with difficult accessibility, which makes reliability important, and maintenance becomes an issue since an unscheduled appointment is excessively expensive. A quantitative example is referenced in [8], where a \$5000 bearing replacement can evolve into a quarter-million-dollar project plus the power generation loss. Also, for a typical turbine with an expected operating life of 20 years, the costs of operation, component replacements, and maintenance, already cover between 10-15% of the total generation income.

As observed, detecting and isolating faults as early as possible is crucial to prevent undesired results and apply the necessary actions on time, which has acted as an initial motivation for this project. Maintenance systems are required, so condition monitoring (CM) and fault detection algorithms are needed. Those can help reduce maintenance costs, minimize unplanned downtime, and extend the lifespan of the turbine. Further, controlling the Cost of Energy (COE) and formulating optimized Operations and Maintenance (O&M) strategies can improve the wind turbine's performance and reduce its energy cost [4]. This will also decrease maintenance costs and make wind energy more commercially competitive [5].

Condition Monitoring (CM) is the process of monitoring a parameter (e.g., temperature) to detect a significant change that could indicate a developing failure [9]. According to [10] fault detection is defined as "the process of detecting, isolating, and identifying a fault in a system through condition monitoring, using techniques such as signal processing or data analysis". As previously mentioned, there are many types of faults that can occur on a wind turbine depending on manufacturing defects, deterioration or damage from components, environmental factors, and more. The severity of those is another

concept to consider since it can vary from a minor issue to a major problem that can result in repairs or even a total wind turbine shutdown. The main objective is to primarily focus on identifying faults that have the potential to cause a complete shutdown of the wind turbine.

1.1 Control Cabinets

A wind turbine consists of the main structures of the foundation, the tower, the rotor and hub (including blades), and the nacelle. The nacelle is located at the top of the tower and contains the most important components of the turbine, including the yaw system, main-shaft bearing, gearbox, generator, and electrical control cabinets that enable the turbine to generate electricity [11].

A control cabinet is an enclosure unit that contains electrical components such as control systems, power electronics, or other machinery to regulate and manage the produced electricity by the generator. These may differ in size, the components integrated, and configuration, depending on the specific design and application of the wind turbine. Large wind turbines, such as offshore, have a more complex design, hence they require larger control cabinets. They are usually equipped with temperature sensors and cooling fans.

The electrical system in the cabinet generates heat as a result of operating, therefore, the fans' function is to circulate the air inside to dissipate the generated heat and prevent overheating. The inlet fan, usually located at the bottom of the cabinet, will draw cool air from the outside and, the outlet fan, located at the top, will push out the heated air. As observed, it is essential that the temperature is managed correctly, and it remains within the operational limits of the components. Failing to manage the temperature within the manufacturer's rated temperature can lead to component failure, decreasing the efficiency, damaging the equipment, and eventually leading to component failure that can result in an unexpected turbine shutdown. For that reason, it is fundamental to have solid fault detection algorithms to identify an abrupt increase in temperature, which can indicate an occurring fault in the system.

Chapter 2

Problem Analysis

Temperature management plays a crucial role in assuring the optimal performance and reliability of control cabinets and their components, which are sensitive to temperature fluctuations. Despite its importance, the existing literature on this specific topic is remarkably limited. Although some work has been done regarding control cabinets and temperature management of wind turbines and the nacelle, an extensive review was done to find the available papers and publications in this area, and it became evident the lack of investigation about temperature management of a control cabinet, which emphasizes the need for further exploration. Though, related topics have been discussed such as temperature management of HVAC systems, indoor climate control of buildings, and different methods of fault detection algorithms for temperature estimation. In this analysis, different methods for temperature control and fault detection algorithms on different scenarios are discussed, and new methods will be proposed.

2.1 State of the art

In [12], et al. Yang developed a model-based optimal indoor climate control for a real-sized livestock stable system. This system applies a single-zone method that uses hybrid ventilation and low-pressure climate strategies and is based on the energy balance and the mass principle. The system is described as a non-linear state space model from which an ideal equilibrium point is calculated, and a linearized model is obtained. Parameter estimation is attained through experiments and only the temperature is considered as a unique control criterion. A constrained MPC is developed and kept the indoor temperature within the required range around the set point, although results show that the indoor temperature (20.5 degrees) is higher than the steady-state temperature at the equilibrium point (20 degrees) due to the outside temperature being higher than its steady-state value (15 degrees). The model is then compared to the real system and shows the feasibility of using a single-zone for optimal climate control.

Another paper [13], et al. Yang and Valente study the viability of improving the

HVAC system for manned offshore oil-and-gas platforms by using an MPC constraint strategy to manipulate the inlet opening area to control the indoor pressure. The single-zone concept is used to model the system where the only controllable input is the inlet opening area A_{in} and the outputs are the indoor temperature T_r and the indoor pressure P_r . The developed controller consists of a Kalman Filter for state estimation and a constraint MPC solution based on estimated states (P_r and T_r). When compared to the previous PID, the controller let the indoor pressure drift away from the expected level – more than 50 Pa over the ambient temperature during 12-15 sec. In comparison, the MPC results in better performance in terms of faster time responses, fewer overshoots, and more robustness to disturbance.

As an extension to the previous paper, [14] proposes a combined feed-forward and a PI-based feedback control solution and an MPC solution to regulate the variable-speed pressurization fan system, by operating the inlet throttle openness of [13], also based on the single-zone concept. The inlet air pressure is assumed constant, assuming that the pressurization control loop via the fan-speed control mechanism is guaranteed. The control solution is developed by combining a static fan model and a feed-forward/feedback system for indoor pressure control. The feed-forward calculates the steady-state fan speed through the indoor pressure and the variable fan speed, subject to the inlet and outlet throttle positions.

Previous methods for fault detection were reviewed in Turner et al. (2017), where a data-driven approach is proposed to automate a building HVAC fault detection relying on parameter estimation based on a computational RLS algorithm used for real-time fault tracking. Depending on the specific faults to be detected, a time-varying ARX or ARMAX model is formulated. By tracking the model parameter values it is possible to detect faults online and in real-time. This approach does not require a detailed physics-based model of the building. Heating and cooling system faults can be detected by simply tracking indoor and outdoor air temperatures [15].

Other investigations regarding fault detection in cabinets have been studied, where Lijun et. al [16] proposed a new method of state detection of a switch cabinet, which combined fuzzy theory with D-S evidence reasoning. Here, temperature and humidity sensors are used to detect the ambient temperature and humidity within the cabinet. Infrared sensors are applied to find the electrical components' temperature which will reflect the heating state as the temperature increases, and ultraviolet sensors are applied to detect the partial discharge of the electrical components. All this data is then fused with the fuzzy theory to reflect the states and make an appraisal of potential faults. The accuracy of the state detection is increased to 92%, while the accuracy of the state detection only by infrared sensors is 79%, and only by ultraviolet sensors is 85%.

2.2 Summary

From a previous project committed in AAU Esbjerg [17], a detection algorithm was applied by using parameter estimation and RLS techniques to detect a fault in a fan within a thermal model of a control cabinet and the nacelle. By calculating some system parameter values, an indication of a fault occurring can be interpreted when these values deviate from the nominal value. The algorithms are tested with the fans working at rates of 90%, 75%, and 0%. There is a proportional correlation between the working rate of the fan and the cabinet temperature, the lower the working rate, the higher the temperature. RLS results showed a temperature deviation of 10% from the expected in all scenarios, suggesting that either the thermal model needs further development, or that the used Forgetting factor requires more precision.

So, inspired by the literature from [17], this project aims to continue with the investigation and work towards an industrialization solution. The simulation model will be based on the single-zone concept in order to fulfill industry requests and align with the desired approach of employing simple model-based FDDs. This model will be expanded to a multi-zone model which will include further thermodynamic properties and will act as validation for the following FDDs. Besides, different fault detection methods will be considered and evaluated for estimating the control cabinet temperature in order to detect a fault in the cooling fans. Furthermore, a parameter estimation process (calibration) will be initiated, from which several proposed model-based FDD methods will be applied. The proposed FDDs for this project will include a simple bank of observers, an MMAE (Multiple Model Adaptive Estimation) technique based on Liniger et. al [18], as well as the Joint State estimation approach based on Yang et. al [19].

Chapter 3

Task Statement

3.1 Task Statement

Based on the method chosen and described in Chapter 2, the task statement for the ongoing project is: To detect a fault in a cooling fan by analyzing the temperature inside a control cabinet through different FDD algorithms.

3.2 Delimitation

In order to solve the above-stated problem, a thermodynamic model to simulate the control cabinet will be created, based on the single-zone concept, followed by an expansion into a multi-zone model. The procedure and development of both models are described in Chapter 4.

As the next step, a calibration/parameter estimation process will be conducted using the RLS algorithm, only based on the single one. Since the system parameters are unknown, calibration is necessary to identify the system. The estimated parameters from the calibration process will then act as inputs to the different FDD methods, which will consist of a bank of Observers, an MMAE, and a Joint State estimation. The theory of the proposed parameter estimation and fault detection methods will be described in Chapter 5, and the results from the different FDDs will be analyzed, compared, and finally validated by the multi-zone model in Chapter 6.

Chapter 4

Modelling

In this section, a control cabinet setup is described, which has acted as an initial inspiration for the dynamical model formulation. Also, the thermal properties of the single and multi-zone models are explained.

4.1 Setup

The initial design of the control cabinet was developed at the offices of Siemens Gamesa (Brande) as a starting point, to have realistic measurements for the simulation. The cabinet follows a very simple architecture: has dimensions 2m x 1m x 0.8m, is made of steel, and is composed of an electrical heating device (transformer), a temperature sensor and two cooling fans, an inlet, and an outlet. The transformer is located at the bottom centre of the cabinet, and the fans are at opposite extremes from each other, being the inlet fan at the bottom part, and the outlet at the opposite top part of the cabinet. A simple representation of this design is illustrated in Figure 4.1:

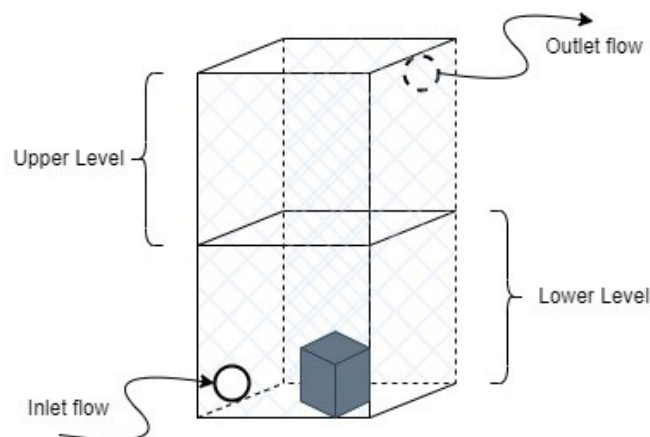


Figure 4.1: Representation of the control cabinet for the multi-zone model

The thermal specifications of these elements as well as the cabinet are described in the following table:

Symbol	Constant	Value	Unit
A_C	Cabinet surface area	8.8	m^2
$c_{p,air}$	Specific heat capacity of air	1005	$\frac{J}{kg \cdot K}$
$c_{p,steel}$	Specific heat capacity of steel	445	$\frac{J}{kg \cdot K}$
$c_{p,cop}$	Specific heat capacity of copper	385	$\frac{J}{kg \cdot K}$
ρ_{air}	Air density	1.255	$\frac{kg}{m^3}$
m_{steel}	Mass of steel	200	kg
m_{steel}	Mass of copper	50	kg
h	Convective heat transfer coefficient	50	$\frac{W}{m^2 \cdot K}$
δ_s	Thickness of the steel wall	0.002	m
k_s	Thermal conductivity of steel	45	$\frac{W}{m \cdot K}$

Table 4.1: Thermal specifications of the model

These values have been gathered through comparison with other industrial control cabinets with similar dimensions. Furthermore, the technical details and the initial conditions of the electrical component and the cooling fans were provided by Frank Vandborg, and have been included in the cabinet design. These conditions specify to work with an air flow range of 200-600 $\frac{m^3}{h}$ generated by the fans, heat generation in a range of 2-5 kW, and a temperature limit set at around 50°C. So, an electrical component that fits these characteristics could be a "TT3 20-4-4" isolating transformer with 20 kVA of rated power [20], and the cooling fans could be a "PF 65SL-Pfannenbergl" with an unimpeded airflow up to 550 $\frac{m^3}{h}$ and area of 0.08 m^2 [21]. Also, a "Pt100" model is the chosen temperature sensor applied in this model, which is a platinum resistance thermometer.

4.2 Single-zone Model

4.2.1 Thermal Dynamics

The dynamical model of the control cabinet system is considered and is under the following assumptions: (1) A single-zone concept is adopted to model the thermal dynamics; (2) The pressures are neglected, and the air is assumed incompressible; (3) The volume flow rate from the fans is constant.

This model is focused on the dynamics of the temperature inside the cabinet. To control the temperature, both the nacelle and the cabinet are considered closed systems, so their energy balance must be conserved. Therefore, the 1st Law of Thermodynamics is implemented, which is based on the conservation of energy, meaning that “energy can neither be created nor destroyed, only altered in form” [22]. A thermal model can be further simulated by obtaining the equations that define the system’s thermodynamic properties. The energy balance equation of a system is the difference between the energy entering and leaving a system and can be expressed as:

$$\Delta E = E_I - E_O \quad (4.1)$$

And the change of energy over time:

$$\dot{\Delta E} = \dot{E}_I - \dot{E}_O \quad (4.2)$$

Where E is the energy.

Since the change of energy over time leads to a change in temperature, the energy balance equation can be defined in a more specific way as follows:

$$c_{p,air} \cdot m_{air} \cdot \frac{dT}{dt} = \dot{Q}_I - \dot{Q}_O \quad (4.3)$$

Where $c_{p,air}$ is the specific heat capacity coefficient of air, m_{air} is the mass of air, \dot{Q}_I is the heat transfer rate into the system, \dot{Q}_O is the heat transfer rate out of the system, and $\frac{dT}{dt}$ is the change of temperature over time.

As mentioned before, the cabinet includes a transformer that will generate heat. So, the energy balance for the project in hand can be inspired by Eq. 4.3 and expanded by considering the effects of the heat generated by the electronic device, the heat transfer from the walls, the heat entering and leaving the cabinet, and some random disturbances. The energy balance for the single-zone model can be expressed as:

$$C_p \cdot \dot{T}_c = \dot{Q}_{in} - \dot{Q}_{out} + \dot{Q}_{heat} - \dot{Q}_{wall} + \dot{Q}_{dist} \quad (4.4)$$

where \dot{Q}_{heat} represents the heat generated by the electrical device, \dot{Q}_{wall} is the heat dissipation through the walls, \dot{Q}_{in} is the heat entering the cabinet through the inlet

fan, \dot{Q}_{out} is the heat leaving the cabinet through the outlet fan, and \dot{Q}_{dist} represents the electronic and ambient disturbances.

The coefficient C_p is the combined heat capacity of the system and is formulated as:

$$C_p = c_{p,air} \cdot m_{air} + c_{p,steel} \cdot m_{steel} + c_{p,copper} \cdot m_{copper} \quad (4.5)$$

This coefficient considers the mass and the specific heat capacity of the air, steel (the material of the cabinet), and copper (the material of the electrical components).

The heat transfer equations described in Eq. 4.4 are represented as:

$$\dot{Q}_{in} = c_{p,air} \cdot \dot{m}_{in} \cdot (T_n - T_c) \quad (4.6)$$

$$\dot{Q}_{out} = c_{p,air} \cdot \dot{m}_{out} \cdot (T_c - T_n) \quad (4.7)$$

$$\dot{Q}_{wall} = \frac{1}{R_t} \cdot (T_c - T_n) \quad (4.8)$$

Where m_{in} and m_{out} are the mass flow of air going in and out of the system, T_n is the nacelle temperature, T_c is the temperature inside the cabinet and R_t is the total thermal resistance, which is explained below. Finally, since the aim is to obtain the change of cabinet temperature over time, the state equation for the system can be expressed as:

$$\frac{dT_c}{dt} = \frac{c_{p,air} \cdot \rho_{air} \cdot (q_{fan,1} + q_{fan,2}) + 1/R_t}{C_p} \cdot (T_n - T_c) + \frac{\dot{Q}_{heat}}{C_p} + w(t) \quad (4.9)$$

where $w(t)$ is the process noise obtained from the division of \dot{Q}_{dist} and C_p , and $q_{fan,1}$ and $q_{fan,2}$ are the volume flow rate generated by the inlet and outlet fan, respectively.

Thermal Resistance

The total thermal resistance (R_t) is used to measure the heat dissipation through the walls. Thermal resistance is a property that measures the temperature difference to which a material resists a heat flow. In other words, represents the resistance to heat flow through a material or combination of multiple layers. So, R_t is the sum of all the individual thermal resistances, each one of them representing a specific layer or material [23]. For this model, the heat flow is across a plane wall of uniform thickness, where R_t is expressed by the equation:

$$R_t = R_{cond} + R_{conv} \quad (4.10)$$

where R_{cond} is the thermal conduction, and R_{conv} is the thermal convection. This equation considers the thermal resistances of all the wall's individual layers and the system's heat transfer interfaces. It splits the wall into different thermal resistance sections and

calculates the thermal conductivity of the material and the convection heat transfer from both sides of the wall [24].

From Eq. 4.10, the thermal conduction and convection values can be calculated from:

$$R_{cond} = \frac{\delta_s}{k_s \cdot A_c} \quad (4.11)$$

$$R_{conv} = 2 \cdot \frac{1}{h \cdot A_c} \quad (4.12)$$

where A_c is the cabinet area, h is the convective heat transfer coefficient of air, δ_s is thickness of the steel wall, and k_s is the thermal conductivity of the steel wall.

As seen, the total thermal resistance is composed of three resistances: the convection heat transfer between the air and the wall on both sides of the cabinet, and the conductivity of the wall itself. Since the air properties are assumed identical inside and outside the cabinet, the convection transfer is the same on both sides of the wall.

4.2.2 Simulation

In this section, the single-zone model has been fed with different step inputs and initial conditions to verify that the thermal properties and dynamics of the cabinet are reasonable since no real temperature measurements were available for comparison.

For both models, the single and multi-zone, the sampling time is set to 1 second due to the temperature sensor specifications. Also, the variance for the measurement noise is set to $\sigma_v^2 = 0.001$, and the variance for the process noise, which was an arbitrary guess, is set to $\sigma_w^2 = 10^{-7}$.

The initial condition for the first simulation consists of the cabinet temperature set at 25°C and the following inputs: $T_n = 25^\circ\text{C}$, $q_{fan,1} = q_{fan,2} = 600\text{m}^3/\text{h}$ and $Q_{heat} = 5\text{kW}$. The cabinet temperature settles at 33°C after 15 minutes. This is a reasonable value for T_c since it is expected to be above T_n without surpassing the operational limits.

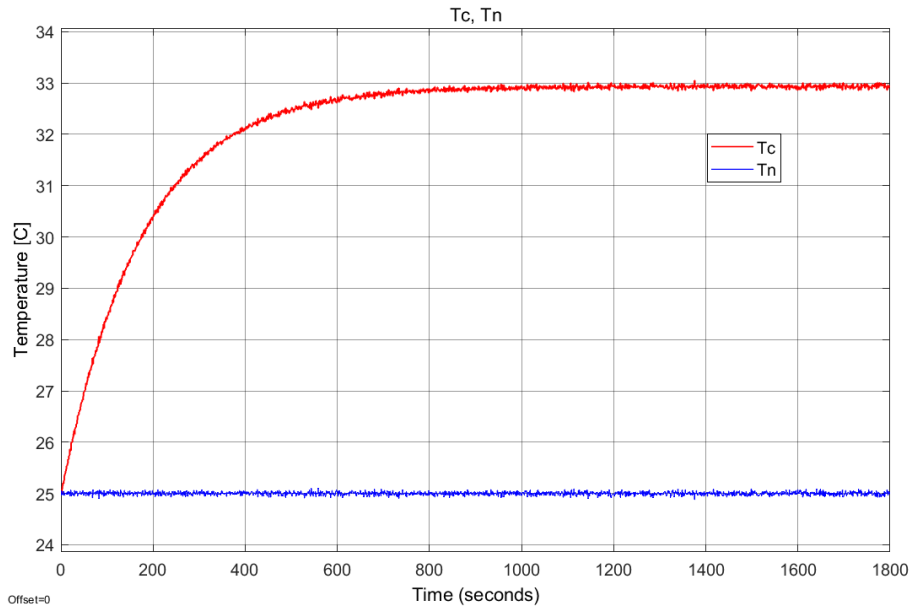


Figure 4.2: Cabinet temperature simulation with inputs: $T_n=25^\circ\text{C}$; $q_{fan}=600\text{m}^3/h$; $Q_{heat}=5\text{kW}$

This next simulation consists of the cabinet temperature set at 50°C and the following inputs: $T_N=25^\circ\text{C}$, $q_{fan,1}=q_{fan,2}=600\text{m}^3/h$ and $Q_{heat}=0\text{kW}$. Neglecting the heat generated by the transformer causes T_c to rapidly go towards T_n , at around 900 seconds.

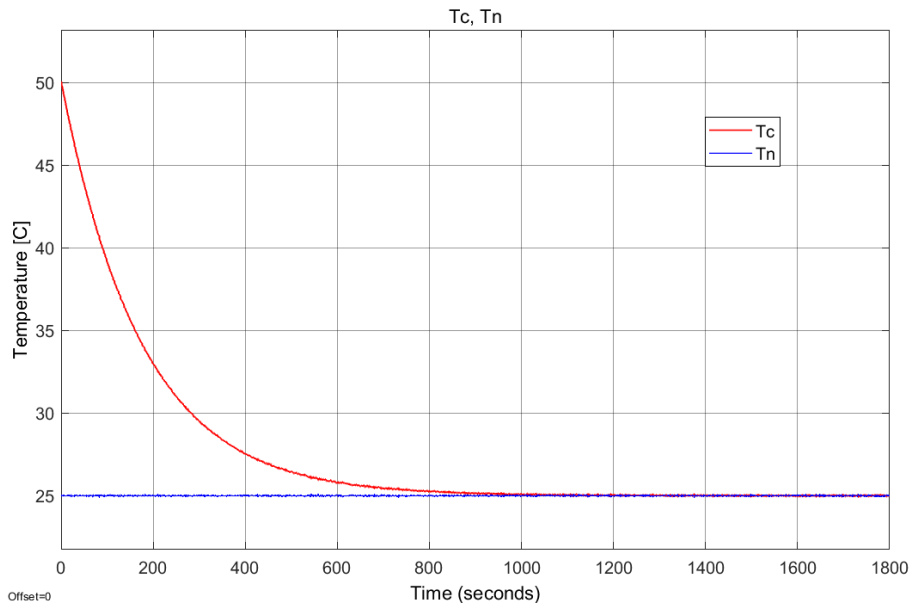


Figure 4.3: Single-zone cabinet temperature simulation with inputs: $T_n=25^\circ\text{C}$; $q_{fan}=600\text{m}^3/h$; $Q_{heat}=0\text{kW}$

The last simulation consists of the cabinet temperature set at 50°C and the following inputs: $T_n = 25^{\circ}\text{C}$, $q_{fan,1} = q_{fan,2} = 0\text{m}^3/\text{h}$ and $Q_{heat} = 0\text{kW}$. Here, the heat is again neglected along with the air circulation generated by the cooling fans. Omitting the cooling ventilation forces the cabinet to only rely on the natural ventilation, and the rate at which T_c approaches the nacelle temperature is more than twice as slow as in the previous simulation, at around 2500 seconds.

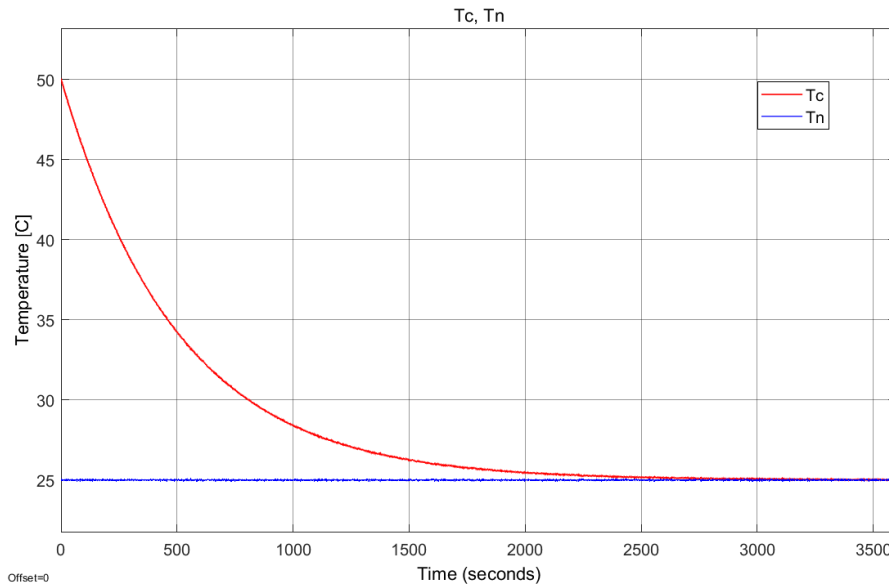


Figure 4.4: Single-zone cabinet temperature simulation with inputs: $T_n = 25^{\circ}\text{C}$; $q_{fan,i} = 0\text{m}^3/\text{h}$; $Q_{heat} = 0\text{kW}$

4.3 Multi-zone model

4.3.1 Thermal Dynamics

This section extends the single-zone model to a multi-zone model by dividing the cabinet into zones. The concept of the zone is used to define control volumes in the model, where the thermal dynamics such as temperature, volume flow rate, density, and other properties, are treated as uniform throughout the zone [25]. This is done to achieve a more realistic system, hence the assumptions from the single-zone are no longer applicable, and concepts such as natural ventilation and thermal buoyancy are added.

Natural ventilation and Thermal buoyancy

Natural ventilation is the process of using natural forces to drive airflow through (in and out) a space, with the purpose of ventilation. It relies on the pressure and temperature difference between the inside and outside to create an airflow. The general objective is

to provide sufficient air from the outside to achieve appropriate air quality standards and is a fundamental technique for reducing energy usage in buildings and rooms [26].

Natural ventilation depends on two natural forces: wind from the enclosing space and buoyancy forces developed due to temperature gradients within the room [27].

If natural ventilation is not sufficient to ensure thermal comfort or its flow rate is too low, the addition of mechanical systems might be needed. This is the concept of “Hybrid ventilation”, which are systems that provide a comfortable cooling capacity using both natural ventilation and mechanical systems, such as fans [28]. There are several ways to achieve natural ventilation such as cross ventilation, single-sided ventilation, or the one treated in this model, stack ventilation.

The stack-effect or buoyancy-driven ventilation is the reaction of the temperature difference between the air inside and outside a room or building to create a flow.

This process is driven by thermal buoyancy, which is the buoyancy force that arises due to temperature differences. This is the natural aftermath of hot air being less dense than cold air, so the warmer fluid will rise and the colder one will sink, creating a flow. So, if the outdoor temperature is lower than the inside, the air that enters the room will warm up, becoming lighter and rising up. This action creates an air movement, where the inside air will escape through the openings at the top of the room [27, 29].

Then, the new model is now divided into two levels - lower and upper. The lower level is composed of the inlet fan (fan 1) and the transformer located at the bottom center of the cabinet, and the upper level is composed only of the outlet fan (fan 2). This is designed according to thermal energy conservation, like the single-zone, with the addition of air mass conservation. The thermal energy from the lower and the upper level are expressed as:

$$C_{p,low} \cdot \dot{T}_l = \dot{Q}_{in,l} - \dot{Q}_{out,l} + \dot{Q}_{heater,l} - \dot{Q}_{wall,l} + \dot{Q}_{dist,l} \quad (4.13)$$

$$C_{p,up} \cdot \dot{T}_u = \dot{Q}_{in,u} - \dot{Q}_{out,u} + \dot{Q}_{heater,u} - \dot{Q}_{wall,u} + \dot{Q}_{dist,u} \quad (4.14)$$

where T_l and T_u denote the lower and upper level temperature, respectively. It can be observed that the total heat capacities $C_{p,low}$ and $C_{p,up}$ are specific to each level since they will be affected by the air mass m_l and m_u .

$\dot{Q}_{in,l}$ in Eq. 4.13 is the heat transfer rate into the lower level through the inlet and it is modeled as

$$\dot{Q}_{in,l} = c_{p,air} \cdot \rho_{low} \cdot q_{in} \cdot (T_n - T_l) \quad (4.15)$$

where q_{in} is the flow rate through the inlet at the lower level. Once the inlet flow rate is estimated, the lower mass flow rate $\dot{m}_{in,l}$ can be calculated by $\dot{m}_{in,l} = \rho_{low} \cdot q_{in}$.

Similarly, $\dot{Q}_{out,u}$ in Eq. 4.14 is the heat transfer rate leaving the upper level through the outlet and it is expressed as

$$\dot{Q}_{out,u} = c_{p,air} \cdot \rho_{up} \cdot q_{out} \cdot (T_u - T_n) \quad (4.16)$$

where q_{out} is the flow rate through the outlet at the upper level. Again, once the outlet flow rate is estimated, the upper mass flow rate $\dot{m}_{out,u}$ can be calculated by $\dot{m}_{out,u} = \rho_{up} \cdot q_{out}$.

Normally, a fan curve from the cooling fans is provided, where the relation between the air volume flow and the pressure is compared. Since this was not supplied and to simplify the calculations, the total flow is defined as a superposition of the air flow generated by the fans ($q_{fan,i}$) and the natural ventilation effect ($q_{nat,in}$ and $q_{nat,out}$). So, the inlet flow can be described as:

$$q_{in} = q_{fan,1} + q_{nat,in} \quad (4.17)$$

where $q_{fan,1}$ is the flow rate generated by the inlet fan (fan 1) and $q_{nat,in}$ is the natural ventilation flow rate through the inlet at the lower level.

Similarly, the outlet flow can be defined as:

$$q_{out} = q_{fan,2} + q_{nat,out} \quad (4.18)$$

where $q_{fan,2}$ is the flow rate generated by the outlet fan (fan 2) and $q_{nat,out}$ is the natural ventilation flow rate through the outlet at the upper level.

To simplify the computational process of the system and conserve the mass principle, it is assumed that the energy leaving the lower level $\dot{Q}_{out,l}$ and the energy entering the upper level $\dot{Q}_{in,u}$ is the same. This section is treated as a boundary layer between the zones and expressed as

$$\dot{Q}_{out,l} = \dot{Q}_{in,u} = c_{p,air} \cdot q_b \cdot \rho_{low} \cdot (T_l - T_u) \quad (4.19)$$

where q_b is the volume flow rate at the boundary layer.

The thermal dissipation through the walls is estimated by

$$\dot{Q}_{wall,l} = \frac{1}{R_{t,l}} \cdot (T_l - T_n) \quad (4.20)$$

$$\dot{Q}_{wall,u} = \frac{1}{R_{t,u}} \cdot (T_u - T_n) \quad (4.21)$$

where $R_{t,l}$, A_l , and $R_{t,u}$, A_u are the total thermal resistance and area of the lower and upper level, respectively. Again, the calculation of R_t follows the same procedure as the single-zone model. The main difference in the calculation of the wall dissipation is the convective heat transfer coefficient (h_l and h_u) applied on each level.

The thermal energy generated by the transformer is defined as:

$$\dot{Q}_{heater,l} = \dot{Q}_{heater} \cdot f \quad (4.22)$$

$$\dot{Q}_{heater,u} = \dot{Q}_{heater} \cdot (1 - f) \quad (4.23)$$

where \dot{Q}_{heater} is a constant value expressed in Watts. The coefficient f ($0.5 < f < 1$) reflects the assumption that the lower level is more affected by the transformer than the upper, since it is located on the ground floor of the cabinet.

According to the mass balance principle, the conservation of mass for both levels is expressed as:

$$\dot{m}_l = \dot{m}_{in_l} - \dot{m}_b \quad (4.24)$$

$$\dot{m}_u = \dot{m}_b - \dot{m}_{out_u} \quad (4.25)$$

where \dot{m}_b represents the mass flow rate at the boundary layer and can be estimated by $\dot{m}_b = \rho_{low} \cdot q_b$.

It is noticeable that the inlet and outlet heat transfer coefficient from both levels, as well as the boundary layer, are certainly dependent on the flow rate.

Since the natural ventilation principle is considered, the volume flow rate can be calculated through Bernoulli's equation [12]. However, the general form of the equation used to obtain the volume flow considering the airflow from thermal buoyancy, cooling fans, and other driving pressure differences is the Orifice equation [26]. In this particular scenario, the inlet and outlet behavior follow this principle. The inlet flow rate can be modeled as:

$$q_{in} = c_d \cdot A_{fan} \cdot \sqrt{\frac{2 \cdot (P_n - P_l)}{\rho_{low}}} \quad (4.26)$$

where c_d is the discharge coefficient, A_{fan} is the area of the fan, P_n is the nacelle pressure, and P_l is the pressure at the lower level.

The outlet flow rate is estimated:

$$q_{out} = c_d \cdot A_{fan} \cdot \sqrt{\frac{2 \cdot (P_u + P_{bu} - P_n)}{\rho_{up}}} \quad (4.27)$$

where P_u is the pressure at the upper level and P_{bu} is the thermal buoyancy effect on that level.

And finally, the flow rate at the boundary layer is calculated by:

$$q_b = A_{cross} \cdot \sqrt{\frac{2 \cdot (P_l + P_{bl} - P_u)}{\rho_{low}}} \quad (4.28)$$

where A_{cross} is the cross-sectional area of the cabinet, and P_{bl} is the thermal buoyancy effect at the lower level. Here, the discharge coefficient is not applied since the space is considered a cross-section rather than a nozzle or an orifice.

In contrast to the single-zone model, the air is assumed compressible and therefore, the ideal gas law is used to calculate the pressure and the density. The pressure from the nacelle, lower and upper level, is obtained using the following equations:

$$P_n = R_a \cdot \rho_{air} \cdot T_n \quad (4.29)$$

$$P_l = \frac{m_l}{V_l} \cdot R_a \cdot T_l \quad (4.30)$$

$$P_u = \frac{m_u}{V_u} \cdot R_a \cdot T_u \quad (4.31)$$

where R_a is the ideal gas coefficient of air, which is 287 J/kg*K.

From these equations, the level densities can be obtained by dividing the air mass over the volume as:

$$\rho_{low} = \frac{m_l}{V_l} \quad (4.32)$$

$$\rho_{up} = \frac{m_u}{V_u} \quad (4.33)$$

This is known as the density formula, which states that density equals mass over volume. The air mass of the levels can be estimated by integrating the mass flow rate from Eq. 4.24 and 4.25, and the volumes V_l and V_u are assumed constant values.

Finally, the differential pressure due to thermal buoyancy is estimated by

$$P_{bl} = (H_c/2 - H_{inlet}) \cdot g \cdot \rho_{low} \cdot \frac{T_l - T_u}{T_l} \quad (4.34)$$

$$P_{bu} = (H_{outlet} - H_c/2) \cdot g \cdot \rho_{up} \cdot \frac{T_u - T_n}{T_u} \quad (4.35)$$

where H_{inlet} is the height of the inlet fan center, H_{outlet} is the height of the outlet fan center, and H_c is the height of the cabinet which refers to the natural pressure level. This equation represents the buoyant pressure between two vertical points [30, 31].

These thermodynamic equations lead to obtaining the cabinet temperature, which is conditioned to the control volumes of both zones, and can be expressed as:

$$T_c = \frac{T_l \cdot V_l + T_u \cdot V_u}{V_l + V_u} \quad (4.36)$$

4.3.2 Simulation

In this section, following the premises in Section 4.2.2, the multi-zone model has been fed with various step inputs and initial conditions to analyze the reliability of the thermal properties of the system. Two scenarios are considered.

The first scenario is formulated on the initial condition that both lower temperature T_l and upper temperature T_u are set to 25°C, and the inputs to the model are $T_n = 25^\circ\text{C}$, $q_{fan,1} = q_{fan,2} = 600 \text{ m}^3/\text{h}$ and $Q_{heat} = 5 \text{ kW}$.

The model is designed in such a way that the lower zone is considerably influenced by the heat dissipation from the transformer, resulting in higher temperatures compared to the upper zone. For that reason, after 20 minutes, T_l settles at 35.8°C and T_u a couple of degrees below at 34.1°C.

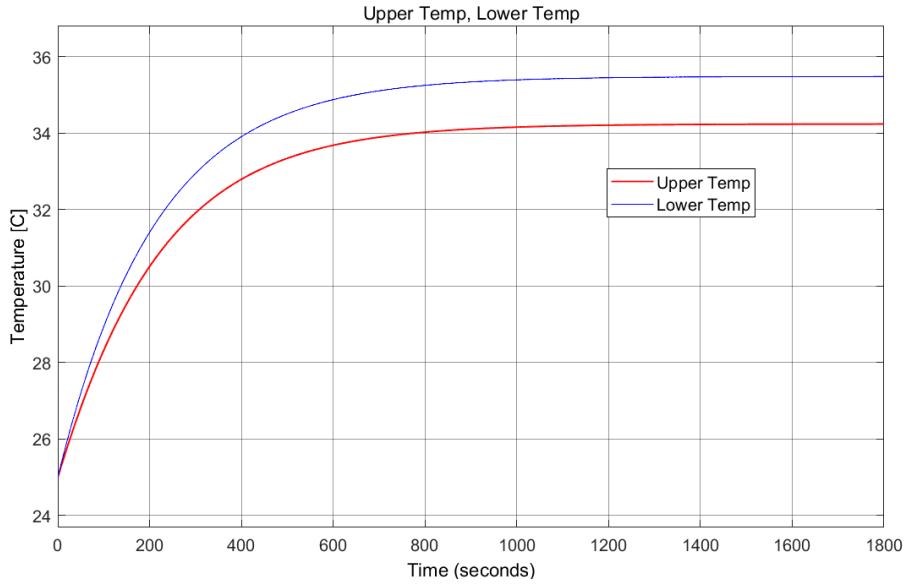


Figure 4.5: Lower and Upper temperature simulation with inputs: $T_n=25^{\circ}\text{C}$; $q_{fan}=600\text{m}^3/\text{h}$; $Q_{heat}=5\text{kW}$

The relation between temperature and density is inversely proportional. For that reason, the upper pressure is slightly above the lower one as anticipated, since the warm air rises to the top of the cabinet due to its lower density, settling after 20 minutes at around 1.0482 bar.

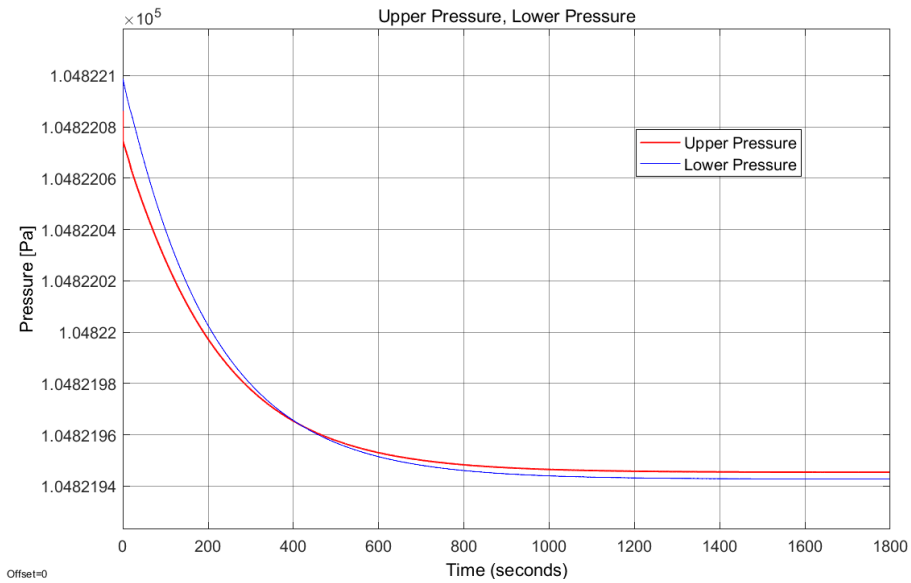


Figure 4.6: Lower and Upper pressure simulation with inputs: $T_n=25^{\circ}\text{C}$; $q_{fan}=600\text{m}^3/\text{h}$; $Q_{heat}=5\text{kW}$

As described in Section 4.3.1, T_c is obtained through the relationship between both

temperature zones and their constant volumes. T_l is assumed to reach a higher temperature than T_u as seen in Figure 4.5. Therefore, T_c is slightly more affected by the lower zone and settles at 35°C after 20 minutes.

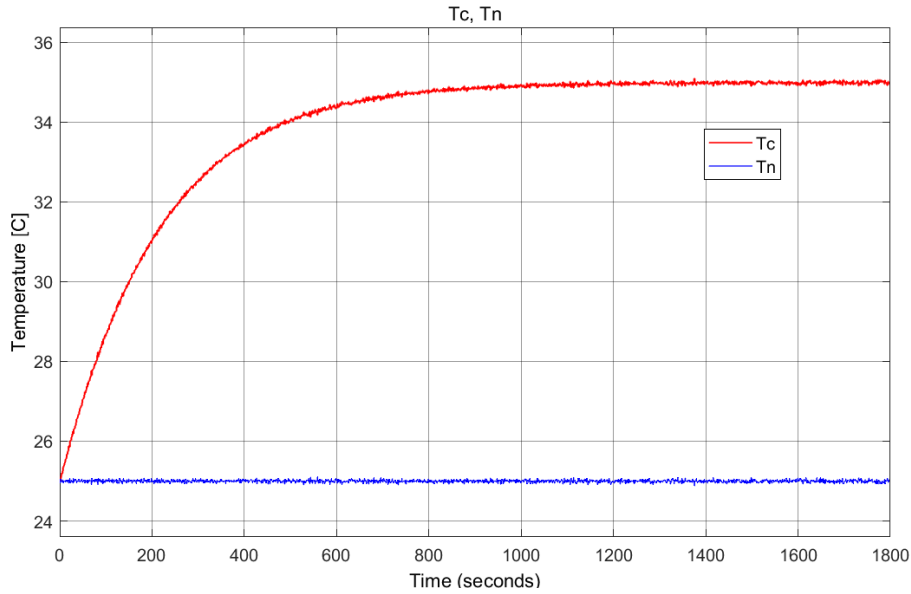


Figure 4.7: Multi-zone cabinet temperature simulation with inputs: $T_n=25^\circ\text{C}$; $q_{fan}=600\text{m}^3/\text{h}$; $Q_{heat}=5\text{kW}$

The second scenario is formulated on the initial condition that the lower temperature T_l is set at 51°C and the upper temperature T_u is set at 49°C . The inputs to the model are now: $T_n=25^\circ\text{C}$, $q_{fan,1}=q_{fan,2}=0\text{m}^3/\text{h}$ and $Q_{heat}=0\text{kW}$.

When the heat dissipation and the air circulation are neglected, the cabinet is forced to rely on natural ventilation to dissipate the air. Here, the temperatures are initially set high, which takes the cabinet temperature 1 hour to settle at the nacelle temperature of 25°C . The lower temperature is assumed to be higher, however, throughout the ventilation process the warm air rises to the top of the cabinet due to its lower density, as seen in Figure 4.6. For that reason, T_u is above T_l while tending towards T_n .

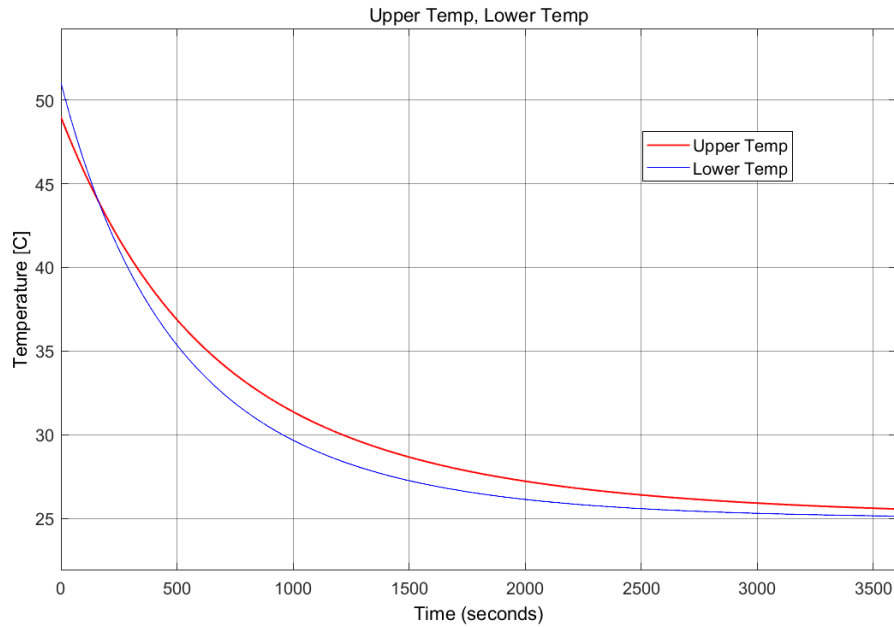


Figure 4.8: Lower and Upper temperature simulation with inputs: $T_n=25^\circ\text{C}$; $q_{fan}=0\text{m}^3/\text{h}$; $Q_{heat}=0\text{W}$

Following the basis of the above Figure 4.8, the cabinet temperature will go towards the nacelle temperature and settle at 25°C after 1 hour.

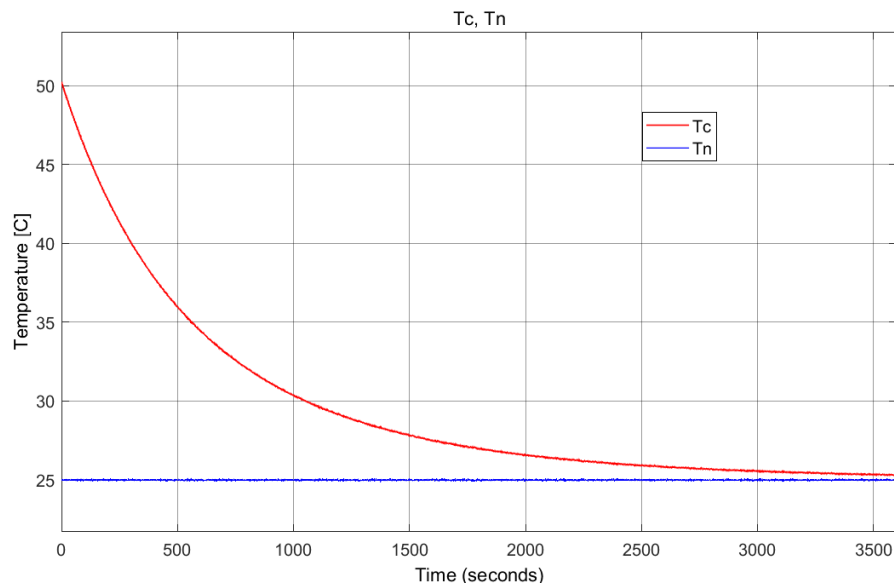


Figure 4.9: Multi-zone cabinet temperature simulation with inputs: $T_n=25^\circ\text{C}$; $q_{fan}=0\text{m}^3/\text{h}$; $Q_{heat}=0\text{kW}$

Chapter 5

Methodology

Prior to presenting the results, the theory behind the proposed parameter estimation technique will be introduced in this chapter, along with an introduction to the state estimation techniques used for the considered FDD methods in this project.

5.1 Parameter Estimation

When the parameters of a system is unknown, parameter estimation methods are typically applied in order to identify the system. A system can be described by the following linear combination in Eq. 5.1.

$$\mathbf{y} = \Phi \cdot \boldsymbol{\theta} + \mathbf{v} \quad (5.1)$$

Here, $\mathbf{y} = [y_1, y_2, \dots, y_l]^T$ is a vector of l number of noisy measurements, $\boldsymbol{\theta} = [a_1, a_2, \dots, a_n]^T$ is a vector of n number of unknown parameters, $\mathbf{v} = [v_1, v_2, \dots, v_l]^T$ is a vector containing the measurement noises and Φ is an $l \times n$ regression matrix containing all the regressor terms of the system [32] [33].

Given an estimate $\hat{\boldsymbol{\theta}}$ the prediction error is described as the difference between the measured output and the estimated output:

$$\boldsymbol{\epsilon} = \mathbf{y} - \Phi \cdot \hat{\boldsymbol{\theta}} \quad (5.2)$$

5.1.1 Least Squares Method

A common approach for estimating unknown parameters is through the Least Squares method (LS). The idea behind this method is to minimize the sum of squared errors given by the cost function $J(\hat{\boldsymbol{\theta}})$, see Eq. 5.3.

$$J(\hat{\boldsymbol{\theta}}) = \boldsymbol{\epsilon}^T \boldsymbol{\epsilon} = (\mathbf{y} - \Phi \cdot \hat{\boldsymbol{\theta}})^T (\mathbf{y} - \Phi \cdot \hat{\boldsymbol{\theta}}) \quad (5.3)$$

Under this principle, the value of $\hat{\theta}$ should minimize $J(\hat{\theta})$. Since this is a second order polynomial, the minimum value for $J(\hat{\theta})$ should satisfy the following equation:

$$\frac{\partial J}{\partial \hat{\theta}} = 0 \quad (5.4)$$

The estimate $\hat{\theta}$ is then achieved by solving for $\hat{\theta}$ in Eq. 5.4, giving the following solution, assuming that $(\Phi^T \Phi)^{-1}$ exists:

$$\hat{\theta} = (\Phi^T \Phi)^{-1} \Phi^T \mathbf{y} \quad (5.5)$$

This is the basic equation for the offline RL method. This requires that all the measurements have already been obtained. More often, however, the measurements are obtained sequentially, and the estimates will need to be updated with each new measurement. This then requires an online parameter estimation approach [32].

5.1.2 Recursive Least Squares (RLS)

For online parameter estimation, a common approach is the recursive least squares method (RLS). As the name indicates, this will recursively compute the estimate from the least squares method. Supposing that a newly obtained measurement \mathbf{y}_k is given by Eq. 5.6.

$$\mathbf{y}_k = \Phi_k \cdot \theta + v_k \quad (5.6)$$

Here, Φ_k is an $m \times n$ regression matrix, where m is the number of measurements contained in one sample, and the noise v_k is assumed to follow a Gaussian distribution with zero mean and covariance R_k , meaning that it will be white noise. In addition to being an online estimation method, RLS also assigns weights to each measurement, which determines the confidence in each individual measurement. These weights are based on the covariance of the measurement noise [32] [33].

The general estimation algorithm for RLS is described by the following equations:

$$K_k = P_{k-1} \Phi_k^T (\Phi_k P_{k-1} \Phi_k^T + R_k)^{-1} \quad (5.7)$$

$$P_k = (I - K_k \Phi_k) P_{k-1} \quad (5.8)$$

$$\hat{\theta}_k = \hat{\theta}_{k-1} + K_k (\mathbf{y}_k - \Phi_k \hat{\theta}_{k-1}) \quad (5.9)$$

Here, K_k is an $n \times m$ gain matrix, also known as a Kalman gain (this will be explained further in section 5.2.2). P_k is the error covariance matrix of the estimate $\hat{\theta}$. Likewise, the term $S_k = \Phi_k P_{k-1} \Phi_k^T + R_k$ corresponds to the error covariance of the estimated output $\hat{\mathbf{y}}_k = \Phi_k \cdot \hat{\theta}_{k-1}$. The RLS algorithm takes into account the statistical properties of the noise and the errors when updating the gain matrix K_k . The idea behind this is to reduce the effect from the measurement noise on the estimate $\hat{\theta}$.

5.1.3 Forgetting Factor Recursive Least Squares (FFRLS)

An extension to the RLS method is the introduction of the forgetting factor λ , where $0 < \lambda \leq 1$. The function of the forgetting factor is to assign more weight to the most recent measurements, thus weakening the influence of older measurements. When $\lambda = 1$, it will weigh all previous measurements equally, meaning that no forgetting occurs. When $\lambda < 1$, the algorithm will have more confidence in the recent measurements and slowly "forget" the older measurements. This is useful if the RLS algorithm needs to adapt to changes in the parameters. The updated RLS algorithm uses the following equations:

$$K_k = P_{k-1} \Phi_k^T (\Phi_k P_{k-1} \Phi_k^T + \lambda)^{-1} \quad (5.10)$$

$$P_k = (I - K_k \Phi_k) P_{k-1} \frac{1}{\lambda} \quad (5.11)$$

$$\hat{\theta}_k = \hat{\theta}_{k-1} + K_k (\mathbf{y}_k - \Phi_k \hat{\theta}_{k-1}) \quad (5.12)$$

Here, the covariance matrix R_k is replaced by λ since the weights need to be updated at each iteration and R_k is normally considered a constant. Depending on the dynamics of the system and the sample rate, the FFRLS algorithm can be highly sensitive to λ , causing it to "forget" too fast, thus resulting in back propagation. As so, λ is usually set to a value close to 1. Other options can include having an adaptable forget factor that will readjust itself based on the prediction error of the output [33].

5.2 State Estimation

Unlike parameter estimation, state estimation considers the unknown values to be the states of the system rather than constant parameters, thus they will be dynamically changing over time. For a linear system, the states can be described through the state space model:

$$\dot{\mathbf{x}}(t) = A\mathbf{x}(t) + B\mathbf{u}(t) + \mathbf{w}(t) \quad (5.13)$$

$$\mathbf{y}(t) = C\mathbf{x}(t) + D\mathbf{u}(t) + v(t) \quad (5.14)$$

Here, $\mathbf{x}(t)$ is the state vector, $\mathbf{u}(t)$ is the input vector and $\mathbf{y}(t)$ is the output vector. $\mathbf{w}(t)$ and $v(t)$ are the process- and measurement noises respectively. A , B , C and D are the state-, input-, output- and feed-forward matrices respectively. The ODE (Ordinary Differential Equation) in Eq. 5.13 is the state equation that describes the dynamics of the system. Eq. 5.14 describes the output of the system. However, $D = 0$ is usually the case, meaning there is no feed-forward interaction. Here, $\mathbf{x}(t)$ contains the unknown states that is to be estimated based on known inputs and outputs of the system.

5.2.1 State Observer

A common way of estimating the unknown states of the system is through a state observer. Assuming no feed-forward in the system, the model of the observer is described by the following equations:

$$\dot{\hat{\mathbf{x}}}(t) = A\hat{\mathbf{x}}(t) + B\mathbf{u}(t) + L(\mathbf{y}(t) - C\hat{\mathbf{x}}(t)) \quad (5.15)$$

$$\hat{\mathbf{y}}(t) = C\hat{\mathbf{x}}(t) \quad (5.16)$$

Here, $\hat{\mathbf{x}}(t)$ is the estimated state vector, $\hat{\mathbf{y}}(t)$ is the predicted output and L is the observer gain matrix. The correction term $\mathbf{y}(t) - C\hat{\mathbf{x}}(t)$ is introduced as a feedback to the observer in order to make the estimation error $\mathbf{e}(t) = \mathbf{x}(t) - \hat{\mathbf{x}}(t)$ converge to zero. The error dynamics of the observer can be derived and reduced to the following:

$$\dot{\mathbf{e}}(t) = (A - LC)\mathbf{e}(t) + (\mathbf{w}(t) - L\mathbf{v}(t)) \quad (5.17)$$

From this equation, it is clear that L needs to be designed in a way that will cause the error dynamics to have stable poles. However, increasing L will also amplify the measurement noise. A rule of thumb is to make the dynamics of the observer five times faster than the dynamics of the system.

5.2.2 Kalman Filter

Another type of state estimation is the Kalman Filter (KF). Unlike a state observer, the KF also considers the statistical properties of the noise in the system. The KF uses an update algorithm similar to the one used in the RLS method, but with the addition of a prediction step. The two steps of the algorithm is shown below.

Prediction Step:

$$\hat{\mathbf{x}}_{k|k-1} = A\hat{\mathbf{x}}_{k-1|k-1} + B\mathbf{u}_{k-1} \quad (5.18)$$

$$P_{k|k-1} = AP_{k-1|k-1}A^T + Q \quad (5.19)$$

Measurement Update Step:

$$K_k = P_{k|k-1}C^T(CP_{k|k-1}C^T + R)^{-1} \quad (5.20)$$

$$\hat{\mathbf{x}}_{k|k} = \hat{\mathbf{x}}_{k|k-1} + K_k(\mathbf{y}_k - C\hat{\mathbf{x}}_{k|k-1}) \quad (5.21)$$

$$P_{k|k} = (I - K_kC)P_{k|k-1} \quad (5.22)$$

Similar to the RLS, the KF includes the measurement noise covariance R , the error covariance P and the Kalman gain K . In the update step of the estimate $\hat{\mathbf{x}}$, the Kalman gain determines how much the algorithm should trust the measurement compared to

the estimated output. This will depend on how noisy the measurements are. If the Kalman gain is approaching the left-side inverse of C , it means that the update algorithm have no confidence in the estimated state and will trust the measurements only. If the Kalman gain is approaching zero, it indicates that the estimated state represents the true state, and only the measurement noise is contained in the prediction error. In the prediction step, the state estimate and error covariance are predicted one step ahead based on the given parameters of the system, where Q is the process noise covariance. It is worth mentioning that the A , B and C matrices are in discrete time for this algorithm.

5.2.3 Extended Kalman Filter

An extension to the traditional KF is the Extended Kalman Filter (EKF). The EKF is used when the system in question is nonlinear. This can be described by the following nonlinear discrete system:

$$\mathbf{x}_k = f(\mathbf{x}_{k-1}, \mathbf{u}_{k-1}) + \mathbf{w}_{k-1} \quad (5.23)$$

$$\mathbf{y}_{k-1} = g(\mathbf{x}_{k-1}, \mathbf{u}_{k-1}) + \mathbf{v}_{k-1} \quad (5.24)$$

For the prediction step, the nonlinear function $f(\hat{\mathbf{x}}_{k-1|k-1}, \mathbf{u}_{k-1})$ is used to predict $\hat{\mathbf{x}}$ at time step k . And $g(\hat{\mathbf{x}}_{k-1|k-1}, \mathbf{u}_{k-1})$ is used to estimate the output. Elsewhere, A and C are replaced by the Jacobian matrices:

$$A_{k-1} = \left. \frac{\partial f}{\partial \mathbf{x}} \right|_{\hat{\mathbf{x}}_{k-1|k-1}, \mathbf{u}_{k-1}} \quad (5.25)$$

$$C_{k-1} = \left. \frac{\partial g}{\partial \mathbf{x}} \right|_{\hat{\mathbf{x}}_{k-1|k-1}, \mathbf{u}_{k-1}} \quad (5.26)$$

The EKF linearizes the system, using the estimate and input at time step $k - 1$ as linearization points. This way, the nonlinear equations can be treated as a linear system at each iteration.

Chapter 6

Results

In this chapter, the procedure behind the development of the calibration and the FDDs will be presented along with the obtained results based on the single-zone model. The optimization of each algorithm will also be described. Finally, the performances of the developed FDDs for the single-zone model will be validated using the multi-zone model.

6.1 Calibration

In Chapter 4, the energy balance equation for the single-zone model resulted in the following state equation:

$$\frac{dT_c}{dt} = \frac{c_{p,air} \cdot \rho_{air} \cdot (q_{fan,1} + q_{fan,2}) + 1/R_t}{C_p} \cdot (T_n - T_c) + \frac{\dot{Q}_{heat}}{C_p} + w(t) \quad (6.1)$$

For the obtained model, the parameters of the system were determined based on information provided by Frank Vandborg from Siemens Gamesa. These parameters include the mass and dimensions of the cabinet, the volume flow rate of the fans and the heat generated by the components inside the cabinet. However, in a real scenario, the algorithm would not have any information about the specific cabinet. Thus, the parameters of the system will have to be estimated during a calibration phase since it is desired to have a universal algorithm that can be applied to any particular cabinet. In order to reduce the number of parameters to be estimated, Eq. 6.1 will be reduced to the following compact form:

$$\dot{T}_c = a \cdot \Delta T + b + w(t) \quad (6.2)$$

Where:

$$a = \frac{c_{p,air} \cdot \rho_{air} \cdot (q_{fan,1} + q_{fan,2}) + 1/R_{total}}{C_p}, \quad b = \frac{\dot{Q}_{heat}}{C_p}, \quad \Delta T = T_n - T_c \quad (6.3)$$

Eq. 6.3 describes a linear relationship between \dot{T}_c and the temperature difference ΔT . Here, a is the "cooling factor" which is a combination of the natural and forced cooling of the system, and b is the heat input. The focus of the calibration is to estimate a and b so that the cabinet system can be identified. These parameters will be estimated using the RLS method described in Section 5.1.2. For the RLS method, the following linear relationship is assumed:

$$\mathbf{y}_k = \Phi_k \cdot \boldsymbol{\theta} \quad (6.4)$$

Where:

$$\mathbf{y}_k = \dot{T}_c(k) \quad \Phi_k = [\Delta T(k) \quad 1] \quad \boldsymbol{\theta} = \begin{bmatrix} a \\ b \end{bmatrix} \quad (6.5)$$

$$\Delta T(k) = T_n(k) - T_c(k) \quad (6.6)$$

Here, \dot{T}_c is obtained using forward Euler:

$$\dot{T}_c(k) = \frac{T_c(k) - T_c(k-1)}{t_s} \quad (6.7)$$

Where $t_s = 1\text{sec}$ is the sample time, and $T_c(k)$ and $T_n(k)$ are the measurements of T_c and T_n , respectively, at time step k . The initial value of $T_c(0)$ for the forward Euler formula is set to 25°C . Since both \dot{T}_c and ΔT are calculated by subtracting the temperatures, the conversion from Celsius to Kelvin is not necessary. $\Delta T(k)$ and $\dot{T}_c(k)$ will then be given as inputs to the RLS algorithm. The calibration is tested on the following scenario for the single-zone model, see Figure 6.1:

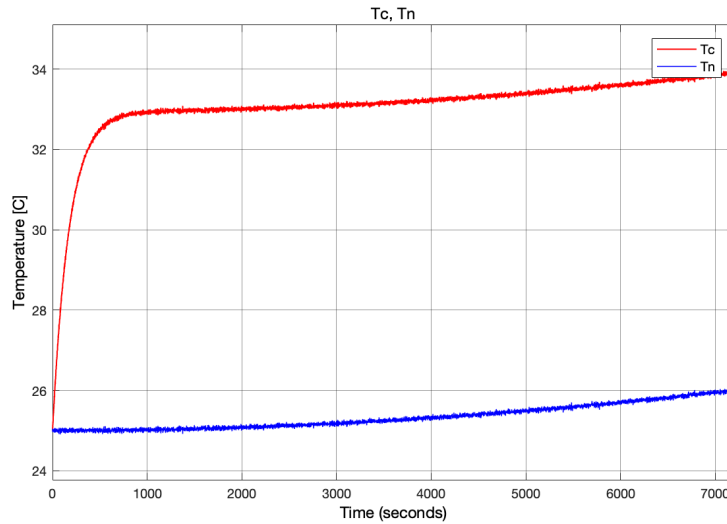


Figure 6.1: Test scenario of healthy system. $\dot{Q}_{heat} = 5\text{kW}$. $q_{fan} = 600\text{m}^3/\text{h}$.

Here, the nacelle temperature is given as a sinusoidal input with a period of one day, where 25°C is the minimum and 40°C is the maximum temperature of the nacelle. The initial conditions of both temperatures are set to 25°C. The cabinet temperature is seen rising in the beginning, indicating some dynamics. After 15 minutes, the cabinet temperature reaches a steady state, where it follows the nacelle temperature. The corresponding training data for ΔT and \dot{T}_c , which is fed into the RLS algorithm, is seen in Figure 6.2.

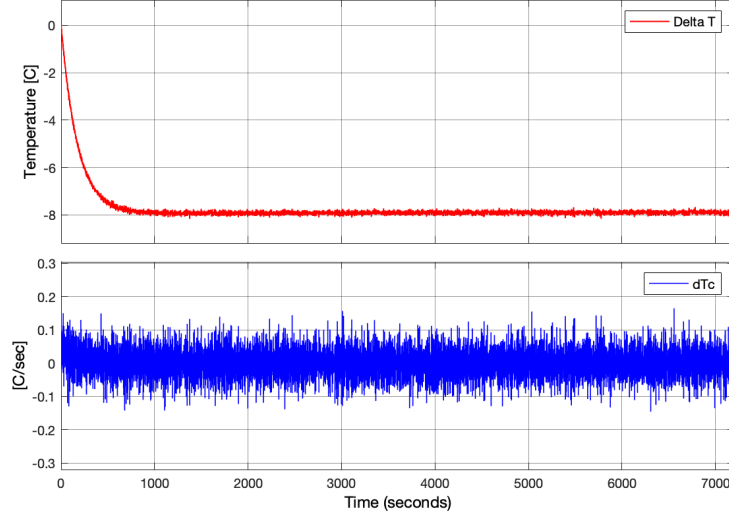


Figure 6.2: Training data for healthy system. $\dot{Q}_{heat} = 5kW$. $q_{fan} = 600m^3/h$.

Since ΔT is calculated using the measured values of T_c , it is sensitive to any noise in the measurements. The calibration uses the following algorithm from Section 5.1.2:

$$K_k = P_{k-1} \Phi_k^T (\Phi_k P_{k-1} \Phi_k^T + R)^{-1} \quad (6.8)$$

$$P_k = (I - K_k \Phi_k) P_{k-1} \quad (6.9)$$

$$\hat{\theta}_k = \hat{\theta}_{k-1} + K_k (y_k - \Phi_k \hat{\theta}_{k-1}) \quad (6.10)$$

Where the covariance is set to $R = 1$ and the initial guesses on the estimate and error covariance are set to:

$$\hat{\theta}_0 = \begin{bmatrix} 0 \\ 0 \end{bmatrix}, \quad P_0 = \begin{bmatrix} 1 & 0 \\ 0 & 1 \end{bmatrix} \quad (6.11)$$

The results of the calibration using the unfiltered training data are illustrated in Figure 6.3.

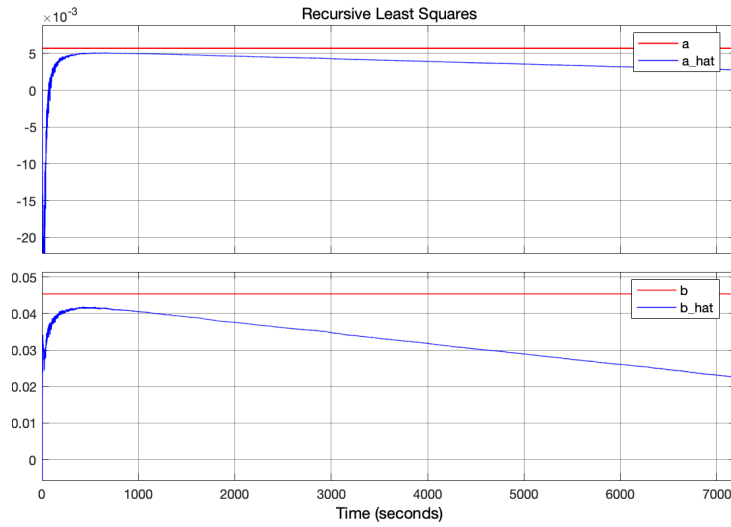


Figure 6.3: Comparison of estimated parameters from RLS vs true parameters of the single-zone model.

The figure shows that the estimated values of a and b will start to drift away from the true values after the system reaches a steady state, since ΔT will settle towards a constant value while \dot{T}_c will keep changing drastically. To account for this noisy training data, a low pass filter is applied to \dot{T}_c which will reduce the noise. The low pass filter is designed using the following discrete transfer function in Simulink:

$$H(z) = \frac{t_s/\tau}{z + (t_s/\tau - 1)} \quad (6.12)$$

Here, τ is the time constant that determines the strength of the filter. The filter allows frequencies below a certain threshold to pass through, and the higher frequencies are filtered out. This threshold depends on the time constant and the sample time. Since this filter is a first-order transfer function, its initial output is zero and it has a rise time before it reaches the correct output. Therefore, the first few data points at the beginning are not used for the calibration as the values are incorrect. The effects of the filtering are seen in Figure 6.4.

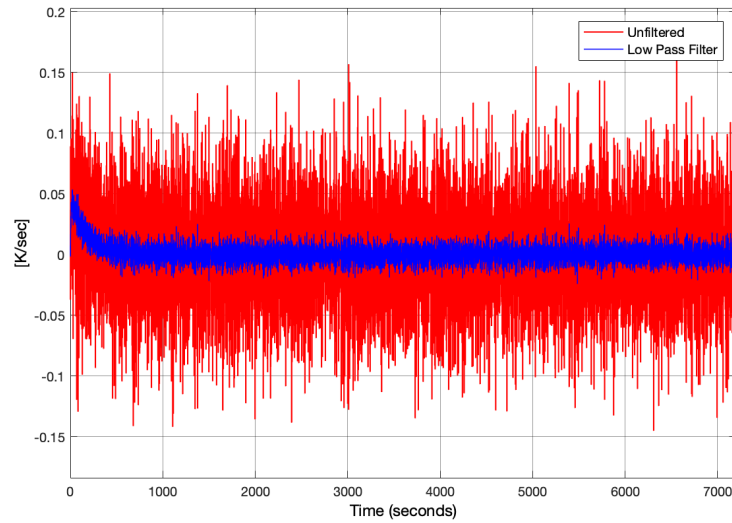


Figure 6.4: Comparison of unfiltered training data vs filtered training data.

Through trial and error, the time constant for this filter has been set to 5 sec, and the first 60 sec of samples will be discarded. This means that the calibration phase is initialized at time $t = 60$. The new training data for the RLS algorithm is seen in Figure 6.5.

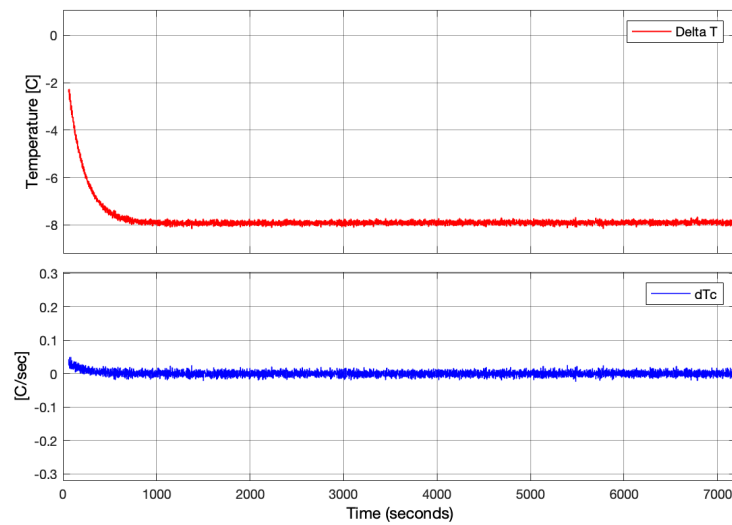


Figure 6.5: New training data for healthy system. $\dot{Q}_{heat} = 5kW$. $q_{fan} = 600m^3/h$.

And the results of the calibration is seen in Figure 6.6.

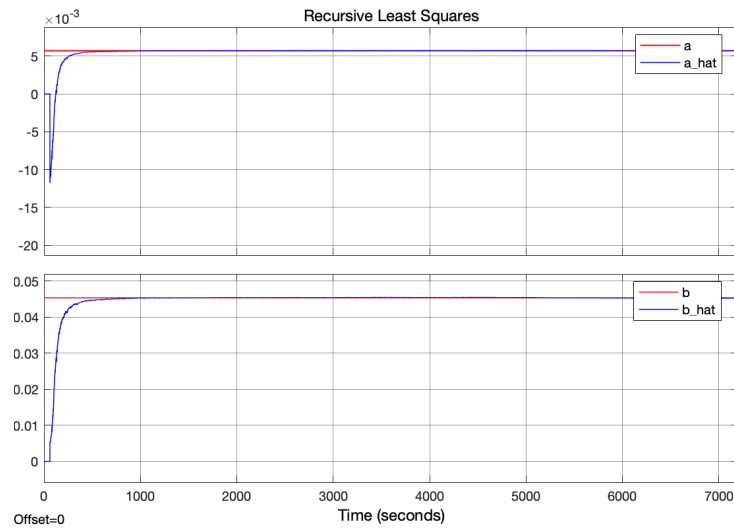


Figure 6.6: Comparison of estimated parameters from RLS vs true parameters of the single-zone model.

Figure 6.6 shows how the estimated parameters rise to the true values during the first 15 minutes, which is where the dynamics are introduced. When looking closer, see Figure 6.7, it can be observed that after the system reaches its steady state, the estimated parameters will start to oscillate around the true values. This is because all future data points collected during the steady state will be stacked on top of each other, creating a cluster of data points with only small variations due to noise. To ensure that the dynamics have a greater impact than the noise, the calibration time is set to 20 minutes, so that only a few data points from the steady state are included. Thus, the calibration will run until the steady state is reached. The estimated parameters from the calibration will then be used for the FDD methods.

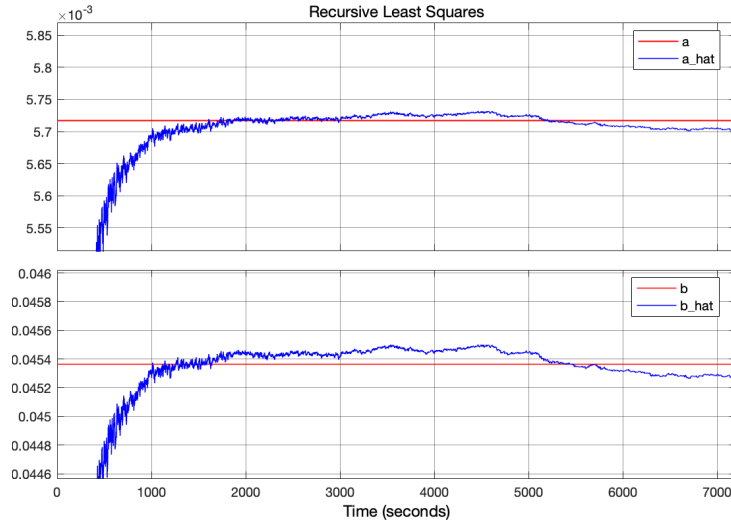


Figure 6.7: Comparison of estimated parameters from RLS vs true parameters of the single-zone model.

6.2 Modelling fault in fans

The focus of this project is to detect faults in the cooling fans in the cabinet. In the model, these faults will affect the performance of the cooling fans, reducing the volume flow rate generated by the particular fan. Thus, each fault can be introduced in the following way:

$$q_{fan,i} = (1 - f_i)q_{nom} \quad (6.13)$$

where, q_{nom} is the nominal volume flow rate of the particular fan type, and f_i is the fault that has occurred to the i th cooling fan. f_i is a value between 0 and 1, where 0 indicates no fault on the cooling fan, and 1 indicates that the fan has stopped.

From Eq. 6.3, the cooling factor a is affected by the volume flow rate of the cooling fans. This means that when a fault occurs in one of the fans, it will cause a to change. Thus, the value of a depends on whether the system is healthy or faulty:

$$a = \begin{cases} a_0, & \text{Normal system} \\ a_f, & \text{Faulty system} \end{cases}$$

a_0 is the cooling factor for a healthy system, and a_f is the cooling factor for a faulty system. The proposed FDD methods in this project will focus on monitoring a and see if its value deviates from a_0 .

6.3 Bank of Observers

The first proposed FDD method is a bank of observers. The idea is to design multiple observers where each of them will represent a "copy" of the real system but under different assumptions regarding the health condition of the cabinet.

Each observer will then try and estimate the states of the real system based on the two temperature measurements. However, since each observer will have different assumptions about the health of the system, they will also have different assumptions regarding the dynamics of the system. Thus, the observer with the best estimation performance is assumed to be the closest representation of the real system.

For the observer design, the cabinet model is described in the following state space form:

$$\begin{bmatrix} \dot{T}_c \\ \dot{T}_n \end{bmatrix} = \begin{bmatrix} -a & a \\ 0 & 0 \end{bmatrix} \begin{bmatrix} T_c \\ T_n \end{bmatrix} + \begin{bmatrix} b \\ 0 \end{bmatrix} \cdot u(t) + w(t) \quad (6.14)$$

$$\mathbf{y}(t) = \begin{bmatrix} 1 & 0 \\ 0 & 1 \end{bmatrix} \begin{bmatrix} T_c \\ T_n \end{bmatrix} + v(t) \quad (6.15)$$

Here, $u(t)$ is considered an input that is either 0 or 1 that indicates if the transformer inside the cabinet is running or not. In the second state equation, the nacelle temperature is modeled as a constant as it is assumed to be slowly varying compared to the cabinet temperature.

Observability

Before designing an observer, it is important to check that the system is observable. This is done by calculating the observability matrix, see Eq. 6.16.

$$O = \begin{bmatrix} C \\ CA \\ CA^2 \\ \vdots \\ CA^{n-1} \end{bmatrix} \quad (6.16)$$

Where n is the number of states. The observability of a system determines how well the internal states can be determined from the external measurements. If the column rank of the observability matrix is equal to n , the system is considered to be fully observable. The observability matrix of the given system is calculated to be:

$$O = \begin{bmatrix} 1 & 0 \\ 0 & 1 \\ -a & a \\ 0 & 0 \end{bmatrix} \quad (6.17)$$

Which is full column rank, meaning that the system is fully observable.

6.3.1 Pole placement

The gain matrix L needs to be designed in a way that will give the observer the desired poles $[\lambda_1, \lambda_2]$ which correspond to the eigenvalues of the observer state matrix. Thus, the desired characteristic equation for the observer becomes:

$$|sI - A + LC| = (s - \lambda_1)(s - \lambda_2) \quad (6.18)$$

By solving L , the desired gain matrix becomes:

$$L = \begin{bmatrix} -(\lambda_1 + a) & a \\ 0 & -\lambda_2 \end{bmatrix} \quad (6.19)$$

As mentioned in Section 5.2.1, a rule of thumb is to make the observer five times faster than the system. The state matrix in Eq. 6.14 has the eigenvalues $[-a, 0]$, thus the first pole of the observer becomes $\lambda_1 = -5a$. However, the second pole should not be zero since this is not a stable pole. To ensure that the observer will also track T_n , the second pole is set to $\lambda_2 = \lambda_1$, meaning that the nacelle temperature error will have the same dynamics as the cabinet temperature error at the expense of being more sensitive to measurement noise. The gain matrix then becomes:

$$L = \begin{bmatrix} 4a & a \\ 0 & 5a \end{bmatrix} \quad (6.20)$$

6.3.2 Observer Design

The bank of observers designed for this project will contain a total of five observers. However, the observers will not know the true value of a and b from the cabinet model. Furthermore, each observer needs to be designed with different values for a based on the assumed health. The general design for the i th observer is described by the following equations:

$$\dot{\hat{\mathbf{x}}}(t) = A_i \hat{\mathbf{x}}(t) + Bu(t) + L_i(\mathbf{y}(t) - C\hat{\mathbf{x}}(t)) \quad (6.21)$$

$$\hat{\mathbf{y}}(t) = C\hat{\mathbf{x}}(t) \quad (6.22)$$

Where:

$$A_i = \begin{bmatrix} -a_i & a_i \\ 0 & 0 \end{bmatrix}, \quad B = \begin{bmatrix} \hat{b} \\ 0 \end{bmatrix}, \quad C = \begin{bmatrix} 1 & 0 \\ 0 & 1 \end{bmatrix}, \quad L_i = \begin{bmatrix} 4a_i & a_i \\ 0 & 5a_i \end{bmatrix}$$

$$\mathbf{y}(t) = \begin{bmatrix} T_c \\ T_n \end{bmatrix}, \quad \hat{\mathbf{x}}(t) = \begin{bmatrix} \hat{T}_c \\ \hat{T}_n \end{bmatrix}$$

Here, \hat{b} is the estimated parameter achieved from the calibration. Likewise, a_i will depend on the estimated "healthy" cooling factor \hat{a}_0 from the calibration as well as the assumed health, see Eq. 6.23.

$$a_i = \hat{a}_0 \cdot h_i \quad (6.23)$$

Where h is the "health factor" defined as:

$$h = \frac{a}{a_0} \quad (6.24)$$

If $h = 1$ then the system is 100 % healthy meaning that the cooling is working as normal. Here, a different value for the cooling factor h will be assigned to each observer. However, $h = 0$ is not considered as it would indicate that there is no cooling in the cabinet, which is not possible for the real system due to the natural cooling. Instead, the considered scenarios are $h = [1; 0.8; 0.6; 0.4; 0.2]$.

6.3.3 Simulation with fault

The FDDs are tested on the same fault scenario in Simulink. For the simulation, the two faults f_1 and f_2 are introduced as step inputs that start from zero. At time $t = 60min$ both faults are set to $f_1 = f_2 = 1$, meaning that both fans will break. The fault simulation is seen in Figure 6.8.

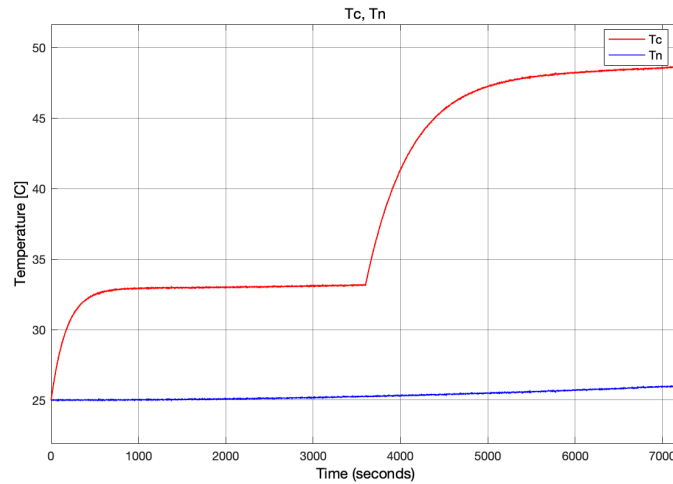


Figure 6.8: Test scenario of faulty system. $\dot{Q}_{heat} = 5kW$

The simulation shows that the system is normal during the first hour i.e. a healthy system. Then, both fans break after one hour resulting in a complete fault. This causes the cooling factor to reduce by 65%. The health factor is seen in Figure 6.9.

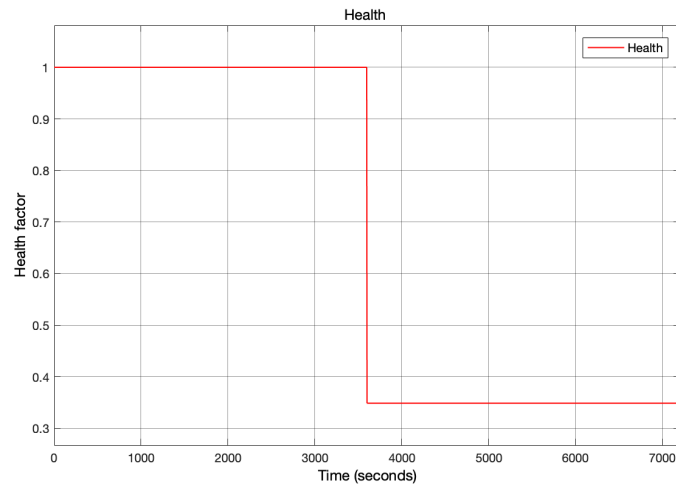


Figure 6.9: Health plot for the fault scenario.

6.3.4 Observer Test

For the FDD tests, the calibration phase and the FDDs are included in the same simulation run. Based on the analysis in Section 6.1, the calibration time is set to 20 minutes to include all the dynamics in the beginning as well as some data from the steady state. After 20 minutes, the calibration will hold the last estimated value of each parameter, see Figure 6.10, and the FDD method is then initialized using both the estimated parameters and the two temperature measurements as inputs.

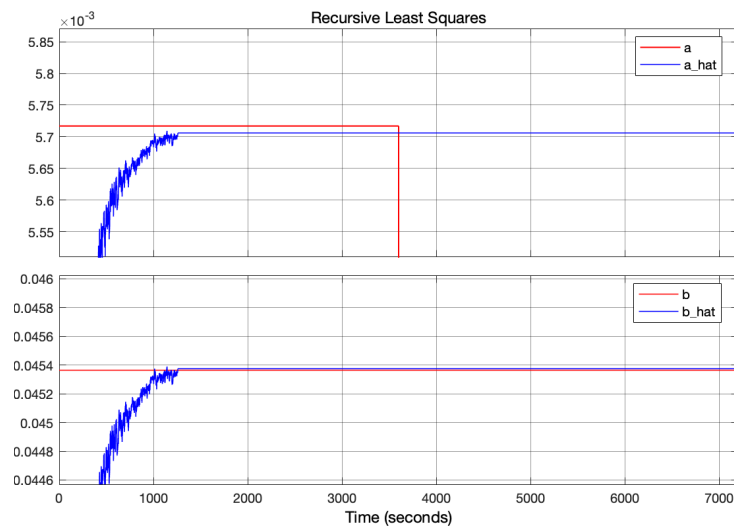


Figure 6.10: Comparison of estimated parameters from RLS vs true parameters of the single-zone model. The true cooling factor "a" is seen to drop when the fault is introduced.

Since both temperatures are measured in discrete time with a sample time of $t_s = 1$ sec, each observer is transformed into the following discrete model:

$$\hat{\mathbf{x}}_{k+1} = A_{d,i}\hat{\mathbf{x}}_k + B_d u_k + L_{d,i}(\mathbf{y}_k - C_d \hat{\mathbf{x}}_k) \quad (6.25)$$

$$\hat{\mathbf{y}}_k = C_d \hat{\mathbf{x}}_k \quad (6.26)$$

Where:

$$A_{d,i} = I + t_s \cdot A_i, \quad B_d = t_s \cdot B, \quad C_d = C, \quad L_{d,i} = t_s \cdot L_i, \quad \hat{\mathbf{x}}_0 = \begin{bmatrix} 30 + 273.15 \\ 20 + 273.15 \end{bmatrix}$$

For each observer, the residual $\mathbf{r}_k = \mathbf{y}_k - \hat{\mathbf{y}}_k$ between the measured output and the estimated output are calculated and will be used to evaluate which observer is the best representation of the cabinet system. The residuals from the five observers are compared in Figure 6.11.

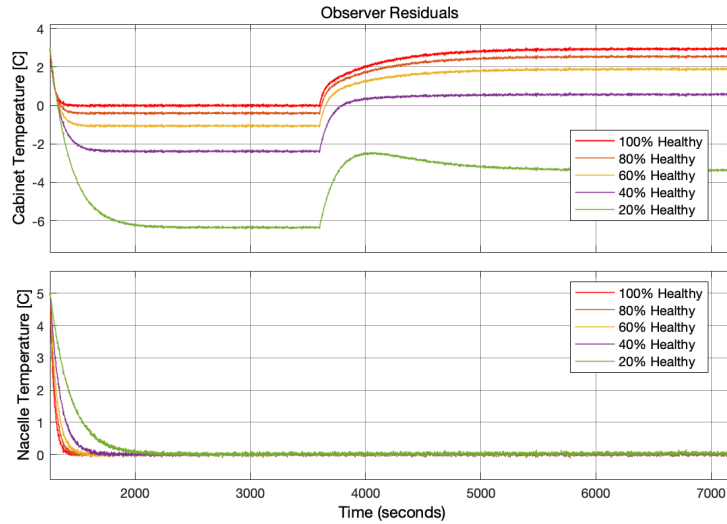


Figure 6.11: Comparison of residuals from the five observers.

Here, the 100% healthy corresponds to the observer with $h = 1$. Likewise, 80% healthy corresponds to $h = 0.8$ and so on. Here, the observers are shown to quickly track the nacelle temperature due to the enhanced error dynamics. It is clear that each observer performs differently when trying to predict the cabinet temperature as each observer makes different assumptions about the cooling based on the assigned value of h . During the first hour, where the system is healthy, the "100% healthy" observer shows the smallest residual i.e. the best prediction. After the fault occurs, the "health" drops to 35%, and the residuals for T_c start to change. After reaching a steady state, the "40% healthy" observer has the smallest residual, indicating that it is now the closest representation of the real system. However, the residual from the "20% healthy" remains

the furthest from zero. Due to the parameters for our particular model, the natural cooling makes up 35% of the total cooling of the cabinet. Thus, the health factor h for this model can never go below 0.35 which makes the last observer redundant for the particular system. In reality, different cabinets will have different sizes, fan types etc. meaning that for a particular cabinet, the natural cooling could potentially make up only 20% of the total cooling (making all observers useful) or 50% (making one or more observers redundant). In order to have a universal FDD algorithm that can be applied to any cabinet without any redundant observers, the "health factor" needs to be redefined. The health factor is instead defined as a normalized value of the cooling factor, see Eq. 6.27.

$$h = \frac{a - \min(a)}{\max(a) - \min(a)} \quad (6.27)$$

Where $\max(a) = a_0$ and $\min(a) = \min(a_f)$. If $h = 1$, the system is healthy. If $h = 0$, cooling has reached its minimum i.e. both fans are broken. The updated health factor for the fault simulation is seen in Figure 6.12.

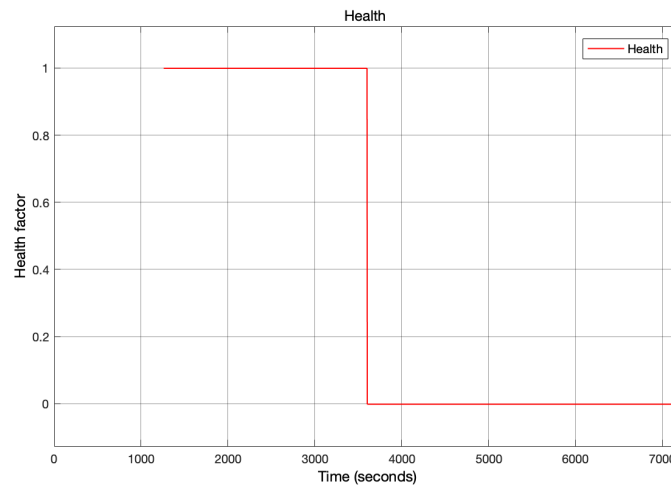


Figure 6.12: Updated health plot for the fault scenario.

For the observer design, a_i is also updated in Eq. 6.28:

$$a_i = (\hat{a}_0 - \min(\hat{a}_f)) \cdot h + \min(\hat{a}_f) \quad (6.28)$$

Here, $\min(\hat{a}_f)$ needs to be obtained through a distinct calibration process prior to the main analysis. For this calibration, both fans are turned off to simulate a fault. By introducing some dynamics into the system, the minimum value of a_f can be estimated, see Figure 6.13 and 6.14.

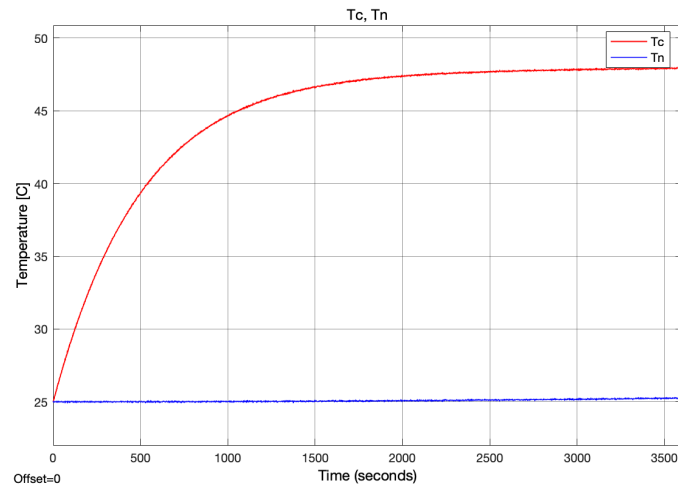


Figure 6.13: Simulation with both fans turned off.

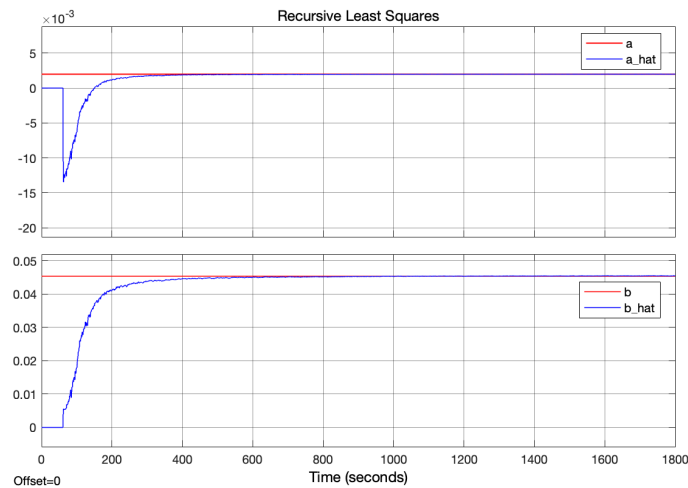


Figure 6.14: Comparison of estimated parameters from RLS vs true parameters of the single-zone model with fans turned off.

Here, the calibration is given 30 minutes to include more dynamics for the training data. It is observed that only a has changed when the fans are turned off, while b remains unaffected.

6.3.5 Results

With the updated definition of the health factor, $h = 0$ can now be considered for one of the observers. The five observers are given the new scenarios $h = [1; 0.75; 0.5; 0.25; 0]$. The updated bank of observers are tested on the same fault scenario as before (from Figure 6.8). The new results of the observer residuals are seen in Figure 6.15.

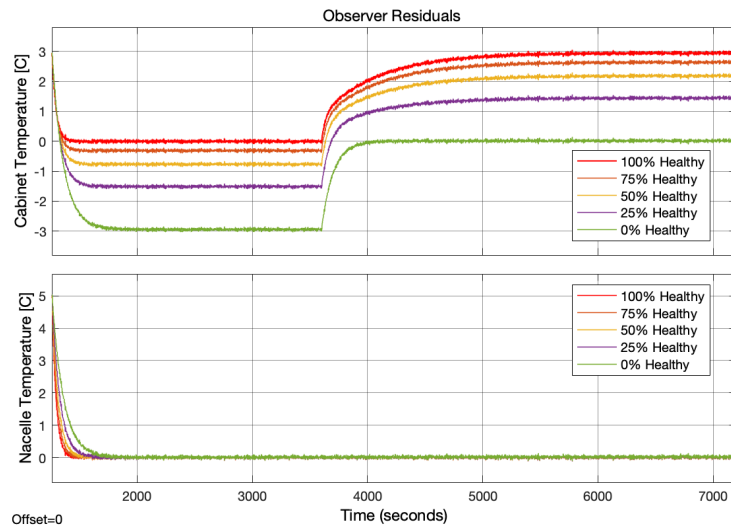


Figure 6.15: Comparison of residuals from the five observers.

These residuals show that the "100% healthy" observer is identical to the real system during the first hour. After the faults occur, the 0% observer becomes the best candidate instead. The residuals of T_c can be further compared by looking at the normalized squared residuals, see Figure 6.16.

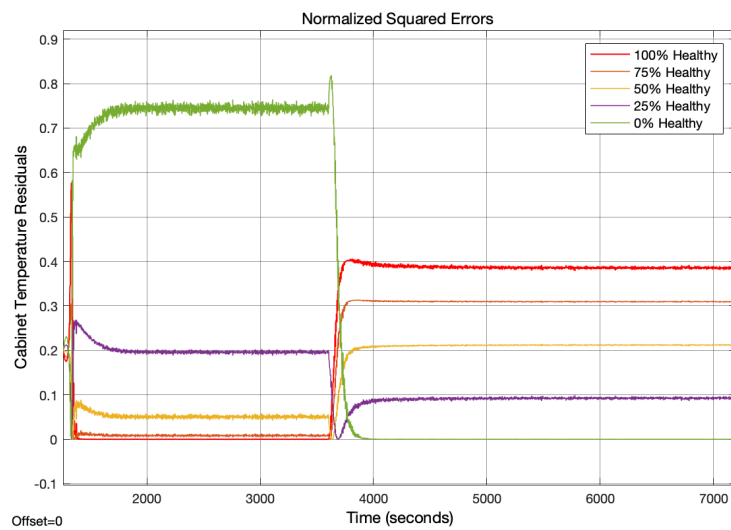


Figure 6.16: Comparison of normalized squared residuals of T_c from the five observers.

Here, each residual is squared and divided by the sum of squared residuals in Eq. 6.29, where the normalized resulting values range between 0 and 1, making them easier to compare and analyze.

$$r_{norm,i} = \frac{r_i^2}{\sum_{j=1}^N r_j^2} \quad (6.29)$$

Where N is the number of observers. Figure 6.16 shows how each residual stands against the other, with the biggest residual being the worst representation of the real system, and the smallest being the best. Here, it makes sense that "20% healthy" would be the second best estimation. The normalized values make it easier to determine in what range, the "health" is located as it would be within the range of the scenario with the smallest residual. Since the observers are designed to quickly track the nacelle temperature, it is not possible to evaluate the residuals of T_n as the estimated outputs are over-fitted to the measurements, see Figure 6.17.

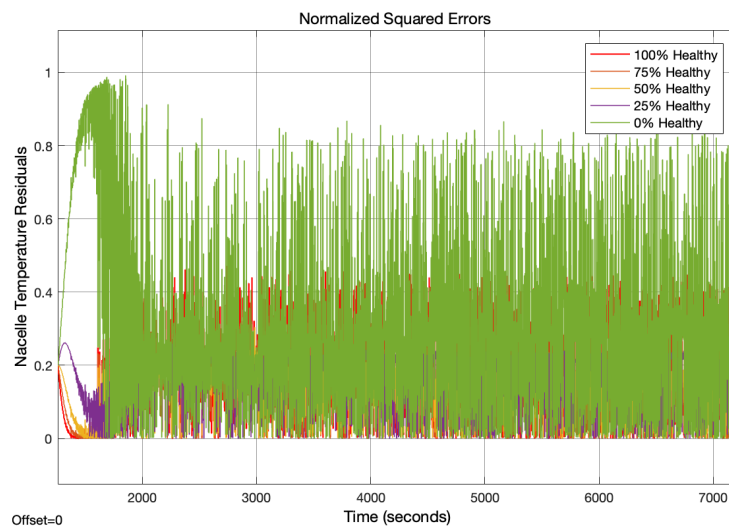


Figure 6.17: Comparison of normalized squared residuals of T_n from the five observers.

This could suggest an alternative model-based FDD method that can evaluate both residuals.

6.4 Multiple Model Adaptive Estimation (MMAE)

Another proposed FDD method is Multiple Model Adaptive Estimation. The first step consists of a bank of Kalman filters, which, unlike the observers, also considers the statistical properties of the noise to increase the accuracy of the estimated states. We recall the algorithm presented in Section 5.2.2:

Prediction Step:

$$\hat{\mathbf{x}}_{k|k-1} = A_d \hat{\mathbf{x}}_{k-1|k-1} + B_d \mathbf{u}_{k-1} \quad (6.30)$$

$$P_{k|k-1} = A_d P_{k-1|k-1} A_d^T + Q \quad (6.31)$$

Measurement Update Step:

$$S_k = C_d P_{k|k-1} C_d^T + R \quad (6.32)$$

$$K_k = P_{k|k-1} C_d^T S_k^{-1} \quad (6.33)$$

$$\hat{\mathbf{x}}_{k|k} = \hat{\mathbf{x}}_{k|k-1} + K_k (\mathbf{y}_k - C_d \hat{\mathbf{x}}_{k|k-1}) \quad (6.34)$$

$$P_{k|k} = (I - K_k C_d) P_{k|k-1} \quad (6.35)$$

The Kalman filters are designed using the same A_d , B_d and C_d matrices as for the observers. The observer gain L is replaced by the Kalman gain K .

6.4.1 Test

The bank of Kalman filters are first tested on a healthy system to see how well it can track the sinusoidal input for T_n using the following process- and measurement noise covariance and initial guesses.

$$R = \begin{bmatrix} \sigma_v^2 & 0 \\ 0 & \sigma_v^2 \end{bmatrix}, \quad Q = \begin{bmatrix} \sigma_w^2 & 0 \\ 0 & 0 \end{bmatrix}, \quad \hat{\mathbf{x}}_{0|0} = \begin{bmatrix} 30 + 273.15 \\ 20 + 273.15 \end{bmatrix}, \quad P_{0|0} = \begin{bmatrix} 1 & 0 \\ 0 & 1 \end{bmatrix} \quad (6.36)$$

It assumes that only the first state equation contains process noise. The results of the residuals are seen Figure 6.18.

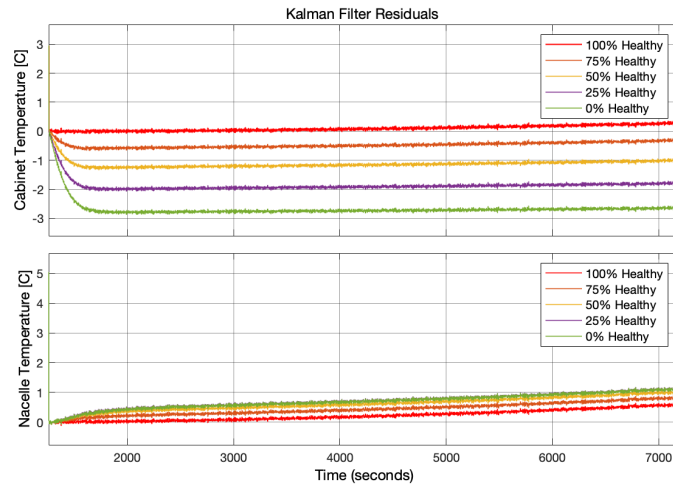


Figure 6.18: Comparison of KF residuals for healthy system assuming no process noise for T_n

It can clearly be observed that both residuals are drifting since the Kalman filters are not accounting for the slow dynamics of T_n . Therefore, the Kalman filters need to include process noise in both state equations:

$$Q = \begin{bmatrix} \sigma_w^2 & 0 \\ 0 & \sigma_w^2 \end{bmatrix} \quad (6.37)$$

The same process noise variance σ_w^2 is assigned to T_n . Figure 6.19 shows the performance of the Kalman filters with the updated covariance matrix.

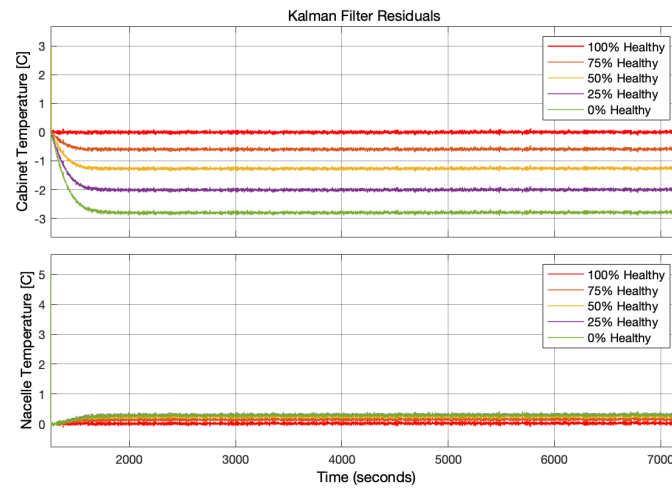


Figure 6.19: Comparison of KF residuals for healthy system assuming process noise for T_n

6.4.2 Results

The bank of Kalman filters are then tested on the same faulty scenario as the bank of observers, recall Figure 6.8. The results are seen in Figure 6.20.

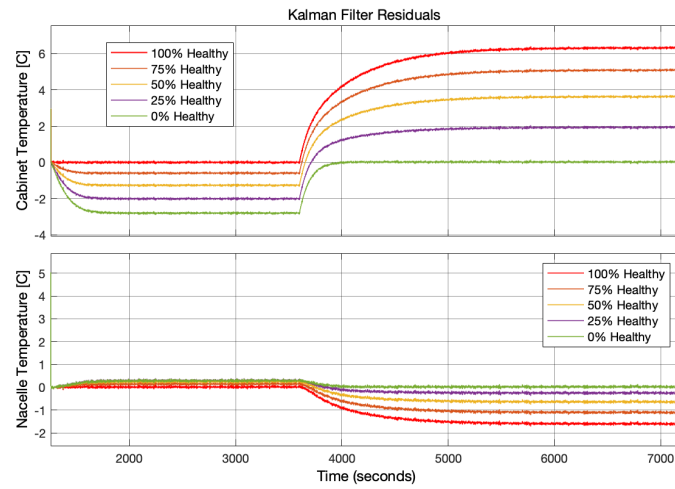


Figure 6.20: Comparison of KF residuals for a faulty scenario.

Here, the residuals of T_n are shown to deviate from each other. The corresponding normalized squared residuals for T_c and T_n are seen in Figure 6.21 and 6.22 respectively.

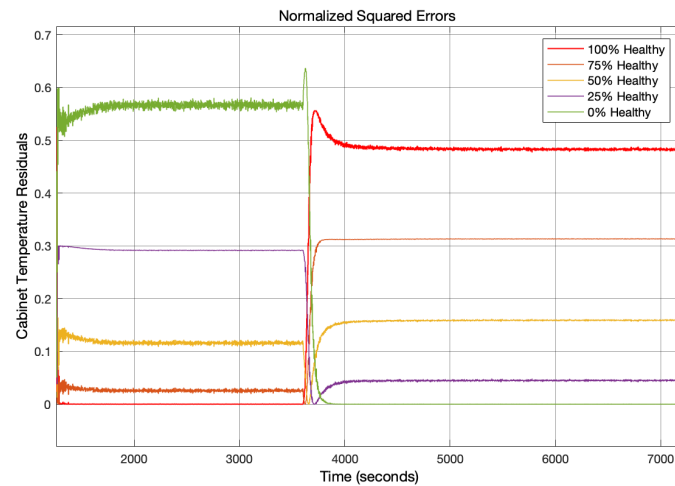


Figure 6.21: Comparison of normalized squared residuals of T_c from KFs.

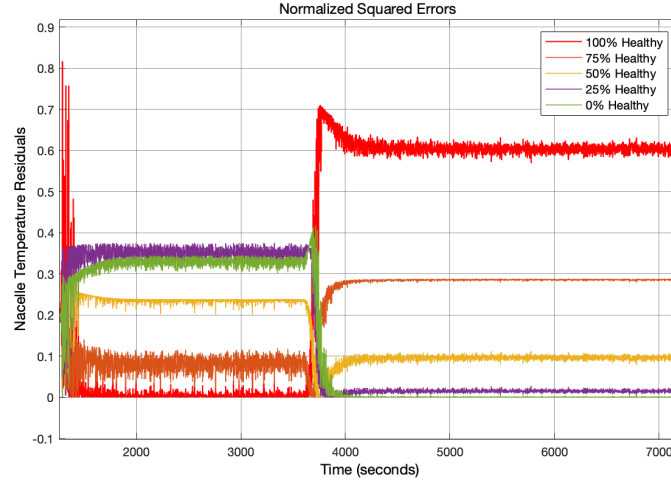


Figure 6.22: Comparison of normalized squared residuals of T_n from KFs.

The two figures show the same outcome as for the observer, with "100% healthy" having the smallest residuals before the faults are introduced, and "0% healthy" having the smallest residuals after the faults have occurred. However, the residuals of T_n only have small deviations from each other in the beginning. This is clear in Figure 6.22, where the residuals for "0%" and "25%" are very similar, and "0%" also appears to be slightly closer to zero than "25%" before the faults occur. The small deviations also cause the normalized residuals to become more noisy. This could suggest that the error covariance S of the residuals needs to be evaluated as well.

6.4.3 Likelihood function

An extension to the bank of KFs is the likelihood function. The MMAE assumes that the real system corresponds exactly to one of the five KF models. It uses the residual vector $\mathbf{r} = \mathbf{y} - \hat{\mathbf{y}}$ together with the covariance S of the residual, assuming normal distribution with zero mean, to calculate the likelihood function, which is the probability density function (PDF) of the residual vector, see Eq. 6.38.

$$l_k = \frac{1}{\sqrt{(2\pi)^n |S_k|}} \exp\left(-\frac{1}{2} \mathbf{r}_k^T S_k^{-1} \mathbf{r}_k\right) \quad (6.38)$$

Where n is the dimension of \mathbf{r} . The likelihood function is then applied to each KF. The five likelihoods are then used to calculate the normalized probability value of each KF using Baye's rule, see Eq. 6.39.

$$p_{i|k} = \frac{l_{i|k} \cdot p_{i|k-1}}{\sum_{j=1}^N (l_{j|k} \cdot p_{j|k-1})} \quad (6.39)$$

The normalized probability values indicate which KF is most likely to correspond to the real system.

In Simulink, the two formulas are expressed in their logarithmic form, see Eq. 6.40 and 6.41, to avoid potential over- and underflow issues when dividing or multiplying with very small or very large numbers.

$$\log(l_k) = -\frac{1}{2}(n \cdot \log(2\pi) + \log|S_k| + \mathbf{r}_k^T S_k^{-1} \mathbf{r}_k) \quad (6.40)$$

$$\log(p_{i|k}) = \log(l_{i|k}) + \log(p_{i|k-1}) - \log\left(\sum_{j=1}^N \exp\left(\log(l_{j|k}) + \log(p_{j|k-1})\right)\right) \quad (6.41)$$

However, this issue is not fully avoided in Simulink. At the time when the fault occurs, all likelihoods will immediately drop to a number very close to zero, see example in Figure 6.23, before slowly increasing. This number is smaller than the smallest representable positive number in Simulink, causing an underflow issue.

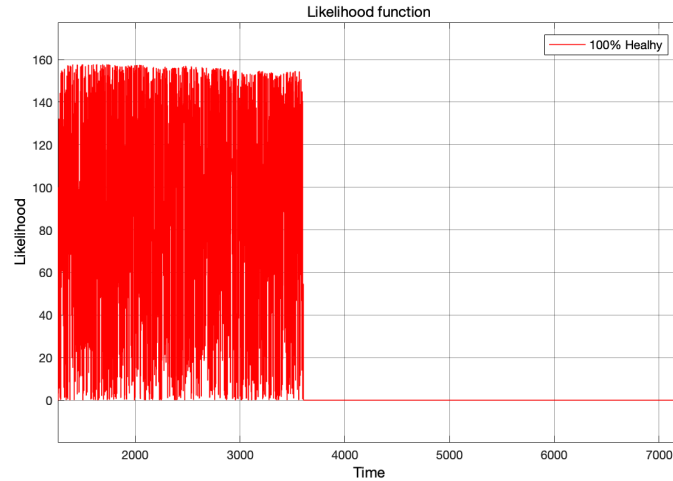


Figure 6.23: Likelihood function for "100% healthy".

In Simulink, it causes the denominator of Eq. 6.39 to be approximated as zero at the given time, and the resulting probability values become "NaN" (not a number). The "NaN" values are then used in the next iteration for Bayes rule, causing the one-step ahead probability value to also become "NaN". This creates a loop where all future probability values will become "NaN" which can not be displayed, see Figure 6.24.

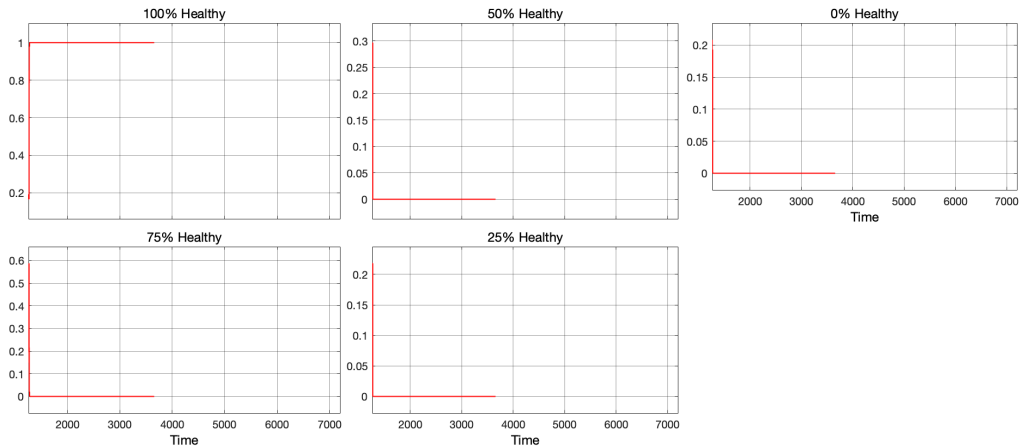


Figure 6.24: Comparison of probability values with underflow issues. Here, the initial value of all five probabilities is set to 0.2 giving them equal probability in the beginning.

To avoid this issue, the five probability values are collected into a vector and given as an input to a MATLAB function. The MATLAB function takes all the elements which are "NaN" and replaces them with 0.2. In other words, each probability is "reset" to its initial value at the time a fault occurs. The "reset" probabilities are then used for the next iteration. The five probabilities are seen in Figure 6.25.

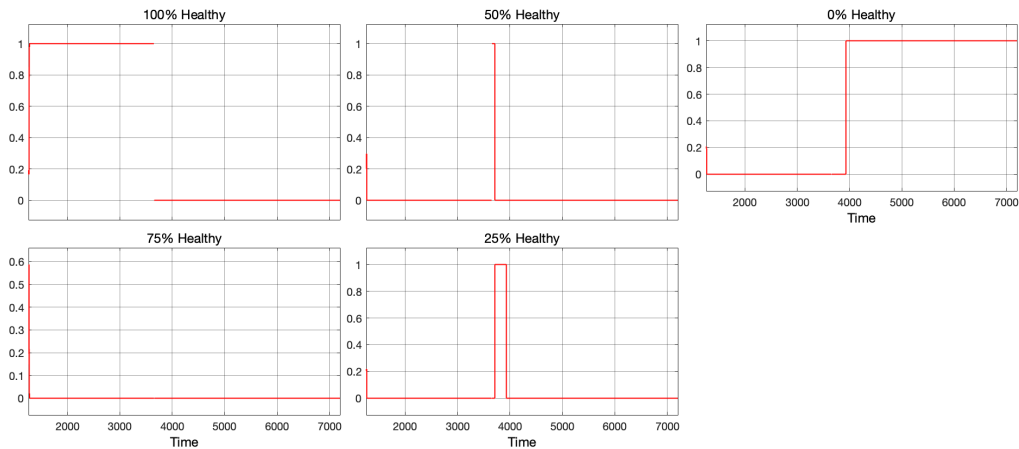


Figure 6.25: Comparison of probability values without underflow issues.

The MMAE shows that the KF representing a normal system (100% healthy) has the best probability of corresponding to the real system before the faults occur. When the faults occur, there is a small transition between each probability as the other residuals from Figure 6.20 are shown crossing zero. Afterward, the KF representing a completely faulty scenario (0% healthy) shows the best probability.

6.5 Joint state estimation

Another proposed FDD method is using an Extended Kalman Filter to directly estimate the cooling factor a . Here, the cooling factor is considered as another state, resulting in the augmented state vector:

$$\mathbf{x} = \begin{bmatrix} T_c \\ T_n \\ a \end{bmatrix} \quad (6.42)$$

This augmented state vector has a nonlinear state equation, due to the joint states, thus the EKF is needed:

$$\dot{\mathbf{x}} = f(\mathbf{x}, \mathbf{u}) + \mathbf{w}(t) \quad (6.43)$$

$$\mathbf{y} = g(\mathbf{x}) + \mathbf{v}(t) \quad (6.44)$$

For the EKF, the Jacobian matrix A :

$$A = \begin{bmatrix} -a & a & T_n - T_c \\ 0 & 0 & 0 \\ 0 & 0 & 0 \end{bmatrix} \quad (6.45)$$

Together with the output matrix C :

$$C = \begin{bmatrix} 1 & 0 & 0 \\ 0 & 1 & 0 \end{bmatrix} \quad (6.46)$$

The A and C matrices are transformed into discrete time using forward Euler, and the following EKF algorithm is applied:

Prediction Step:

$$\hat{\mathbf{x}}_{k|k-1} = f(\hat{\mathbf{x}}_{k-1|k-1}, \mathbf{u}_{k-1}) \quad (6.47)$$

$$P_{k|k-1} = A_d(\mathbf{x}_{k-1|k-1})P_{k-1|k-1}A_d^T(\mathbf{x}_{k-1|k-1}) + Q \quad (6.48)$$

Measurement Update Step:

$$S_k = C_d P_{k|k-1} C_d^T + R \quad (6.49)$$

$$K_k = P_{k|k-1} C_d^T S_k^{-1} \quad (6.50)$$

$$\hat{\mathbf{x}}_{k|k} = \hat{\mathbf{x}}_{k|k-1} + K_k(\mathbf{y}_k - C_d \hat{\mathbf{x}}_{k|k-1}) \quad (6.51)$$

$$P_{k|k} = (I - K_k C_d) P_{k|k-1} \quad (6.52)$$

Where the discrete Jacobian matrix of A is updated at each time step based on the estimate $\mathbf{x}_{k-1|k-1}$.

6.5.1 Observability

However, the observability of the new system equations needs to be evaluated. This is done by checking that the new observability matrix is full column rank:

$$O = \begin{bmatrix} C \\ CA \\ CA^2 \end{bmatrix} = \begin{bmatrix} 1 & 0 & 0 \\ 0 & 1 & 0 \\ -a & a & T_n - T_c \\ 0 & 0 & 0 \\ a^2 & -a^2 & a \cdot (T_c - T_n) \\ 0 & 0 & 0 \end{bmatrix} \quad (6.53)$$

From Eq. 6.53 it is clear that the system is fully observable for $T_c \neq T_n$.

6.5.2 Results

The Extended Kalman Filter is tested on the same faulty scenario from Figure 6.8. The following covariance matrices and initial guesses are used:

$$R = \begin{bmatrix} \sigma_v^2 & 0 \\ 0 & \sigma_v^2 \end{bmatrix}, \quad Q = \begin{bmatrix} \sigma_w^2 & 0 & 0 \\ 0 & \sigma_w^2 & 0 \\ 0 & 0 & 0 \end{bmatrix}, \quad \hat{x}_{0|0} = \begin{bmatrix} 30 + 273.15 \\ 20 + 273.15 \\ \hat{a}_0 \end{bmatrix}, \quad P_{0|0} = \begin{bmatrix} 1 & 0 & 0 \\ 0 & 1 & 0 \\ 0 & 0 & 1 \end{bmatrix} \quad (6.54)$$

The residuals of T_c and T_n from the EKF are shown in Figure 6.26.

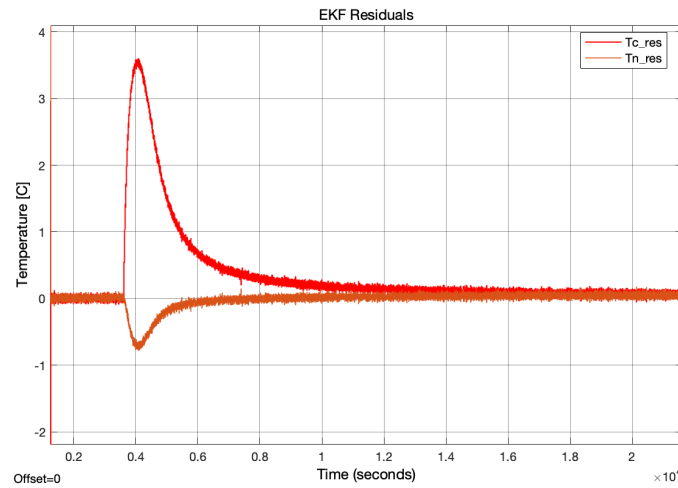


Figure 6.26: EKF residuals of T_c and T_n for a faulty scenario. Simulation time is 6 hours.

The initial guess on the error covariance matrix P causes the residuals to quickly converge to zero in the beginning. P will then settle at a certain value. After the faults occur,

the residuals then slowly converge back to zero, meaning that the estimated outputs are converging towards the true values. This implies that the estimated states can also be trusted. The estimated cooling factor is shown in Figure 6.27 where it is compared to the true cooling factor of the single-zone model.

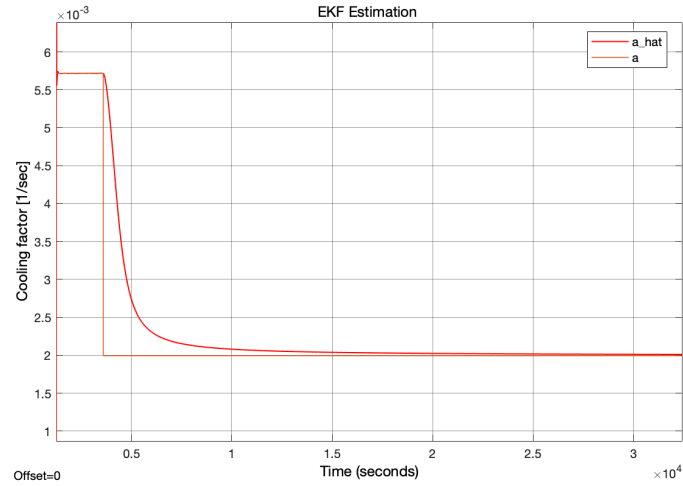


Figure 6.27: Comparison of estimated cooling factor using EFK vs. true cooling factor from single-zone model. Simulation time is 9 hours.

The figure shows the estimated cooling factor slowly converging towards the true value over time. The estimated value \hat{a} is then used together with RLS estimates \hat{a}_0 and \hat{a}_f from the calibration to estimate the health factor of the system, see Eq. 6.55.

$$\hat{h} = \frac{\hat{a} - \min(\hat{a}_f)}{\hat{a}_0 - \min(\hat{a}_f)} \quad (6.55)$$

The estimated health and the true health of the single-zone model are then compared in Figure 6.28

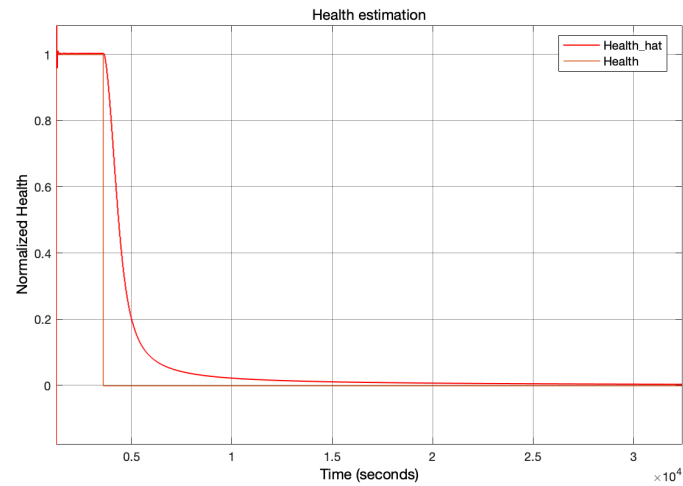


Figure 6.28: Comparison of estimated health factor using EFK vs. true health factor from single-zone model. Simulation time is 9 hours.

The EKF is shown to give a reliable estimate of the "health" of the system over time within some margin of error.

6.6 Validation

6.6.1 Fault scenarios

This section describes the two fault scenarios applied for the multi-zone model fault detection methods.

Scenario 1: Simultaneous failure of both fans

The first scenario mirrors the simulation with faults from the single-zone model, where both faults f_1 and f_2 are set to 1 and introduced as step inputs at time $t = 60min$, meaning that both fans will break simultaneously. The fault simulation can be seen in Figure 6.29.

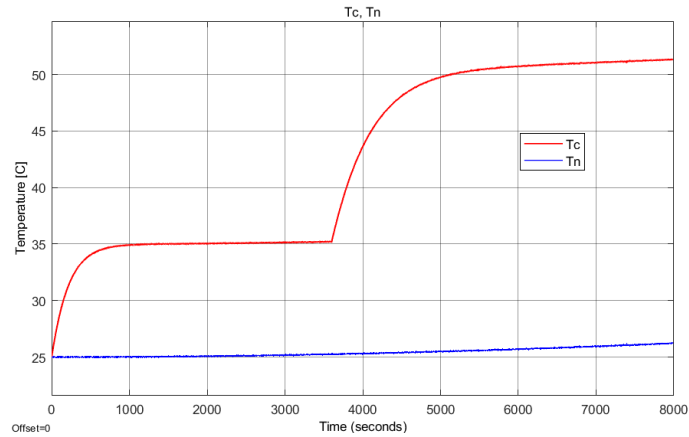


Figure 6.29: Temperature reaction to the faulty scenario 1

The simulation in Figure 6.30 illustrates a healthy system through the first hour, which is reduced to zero as expected after both fans break.

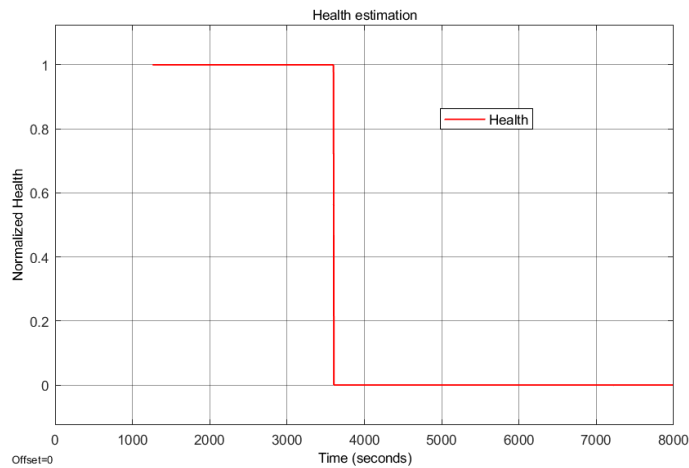


Figure 6.30: Health plot for the faulty scenario 1

Scenario 2: Sequential failure of both fans

In this next scenario, both fans are sequentially set to faulty mode, where f_1 is set at time $t_1 = 60min$ and f_2 is set at time $t_2 = 120min$. The fault simulation can be seen in Figure 6.31.

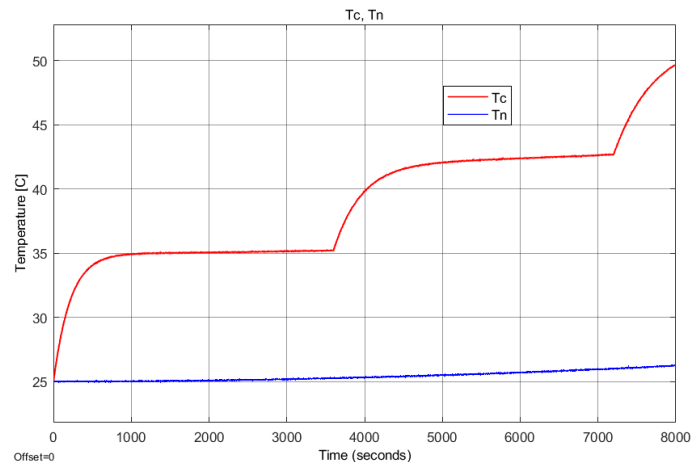


Figure 6.31: Temperature reaction to the faulty scenario 2

From the below plot, Figure 6.32, the health factor visibly declines to 33% when the first fault arises. When the second fault occurs, the health factor drops to zero.

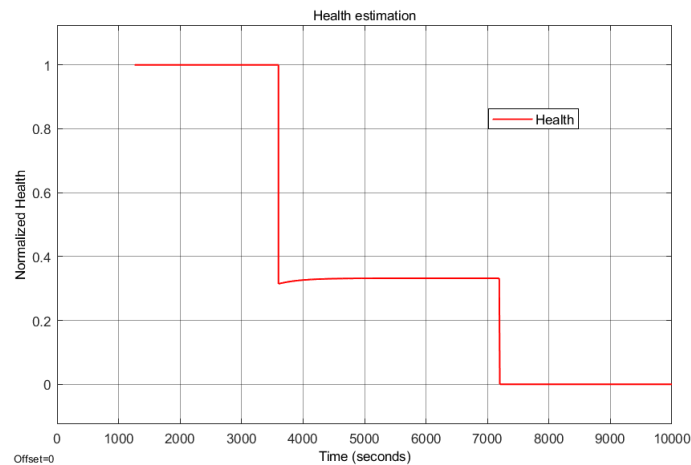


Figure 6.32: Health plot for the faulty scenario 2

After many simulations and different combinations, it can be concluded that the sequence in which the faults are introduced has no impact on the resulting outcome, for both cabinet temperature and health factor.

6.6.2 Calibration

The multi-zone model follows the calibration process described in the single-zone model. In addition, the "forgetting factor" concept was initially introduced in the RLS algorithm to assess the response of the data. It highlights old data compared to the new data

considered spurious, by giving exponentially less weight to the older error samples [34].

The forgetting factor is a very sensitive parameter so, through trial and error, the value was modified by altering the thousandth place in the decimal. Figure 6.33 shows the calibration process with a forgetting factor of 0.999.

It can be observed that estimated values deviate from the true ones. This occurs because the forgetting factor forgets the initial data, where the model dynamics are introduced, and forces the system to rely on the latest measurements which is the steady state. Since the RLS is designed to identify the dynamic behavior of the system, applying constant values from the steady-state, leads to poor performance. For the RLS algorithm to work, dynamics should be introduced throughout the calibration process, which is out of the scope of the present project.

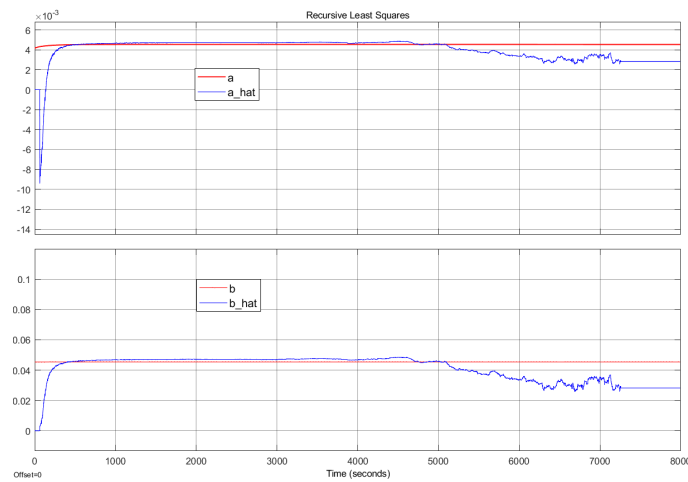


Figure 6.33: RLS algorithm with a forgetting factor of 0.999

In order to address the drifting issue, the forgetting factor value was adjusted to 1, preventing the RLS algorithm from disregarding any information. It can be seen that both estimated parameters rise to the true values after 15 minutes, where the dynamics are introduced, the same way as for the single-zone model in Figure 6.6, although there is an offset with the estimated b due to the complex thermal dynamics.

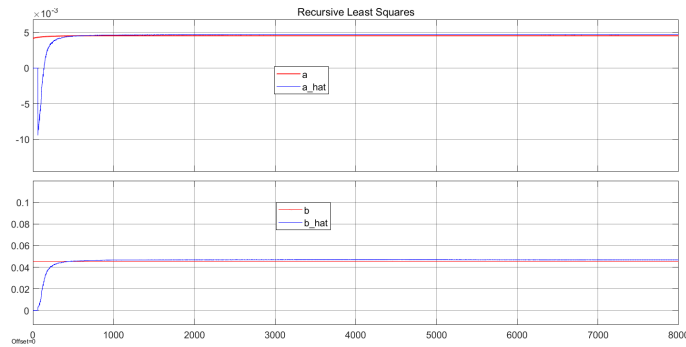


Figure 6.34: Estimation of a and b in the RLS algorithm

The health and performance of the two fans affect the outcome of a , therefore, when both of them are broken, the magnitude of a drops 3 units, and the offset in b increases.

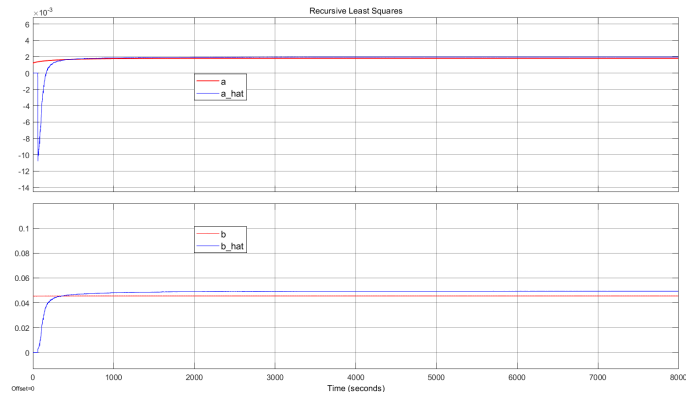


Figure 6.35: Estimation of a and b in the RLS algorithm with both fans off

The following FDD simulations were initialized after reaching the steady state.

6.6.3 Bank of Observers

Similar to the single-zone model, a bank of observers is selected as an FDD method for the study. For the first part of this section, the simulation follows the conditions of *Scenario 1* described in section 6.6.1.

The observer residuals are represented in the following Figure 6.36 and, in a similar manner to Figure 6.15, the "100% healthy" observer resembles the real system in the initial hour. When the fault occurs, the "0% healthy" observer becomes the best prediction of the system.

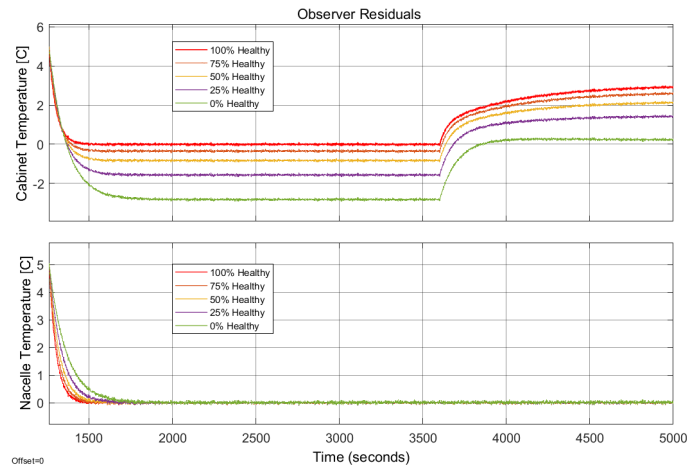


Figure 6.36: Residual comparison from the five observers in the multi-zone model

The normalized squared errors confirm the previous evaluation of the system's progression and tracking of the faults. It can be observed in Figure 6.37 how the "100%" observer remains at zero and, after the fault, the position is switched with the "0%" observer.

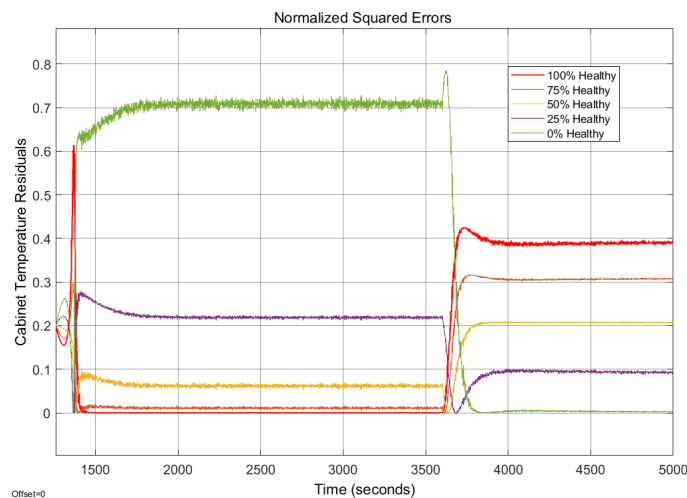


Figure 6.37: Normalized squared errors comparison from the five observers in the multi-zone model

In order to enhance the comprehension of the system and investigate the attributes of the multi-zone model, the faults are now introduced at different times. Here, in Figure 6.38, the simulation follows the conditions of *Scenario 2*. When the first fault occurs after one hour, the best representation of the model is the "25% healthy" observer, which aligns with the health factor dropping to 33% as described in Section 6.6.1. After the second fan breaks, the system is completely faulty, pictured by the "0% healthy" observer

having the lowest residual.

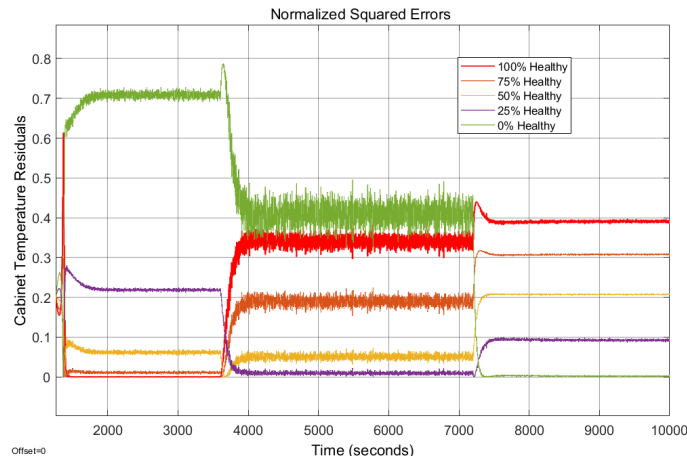


Figure 6.38: Normalized squared errors comparison with two faults in the multi-zone model

6.6.4 MMAE

In this section, a bank of Kalman filter is also considered as an additional FDD method. The simulation follows again the conditions defined in *Scenario 2*.

The KF residuals are defined in Figure 6.39. It is distinctly visible where both faults appear and which observer gives the best prediction, these two being the "25% healthy" and "0% healthy" for the first and second fault, respectively.

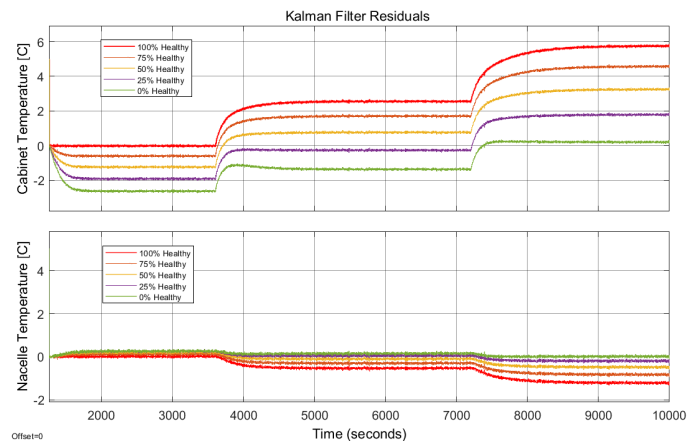


Figure 6.39: KF residual comparison with two sequential faults

The probability of the five KFs is displayed in Figure 6.40, where it can be observed how at the beginning, the best representation of the model is the healthy observer (100% health). After the first fault transpires, there is a transition between the "50% healthy"

and the "25% healthy" observers, being the last one the best prediction. Finally, when the second fault occurs, the "0% healthy" observer is the best candidate for representing the model.

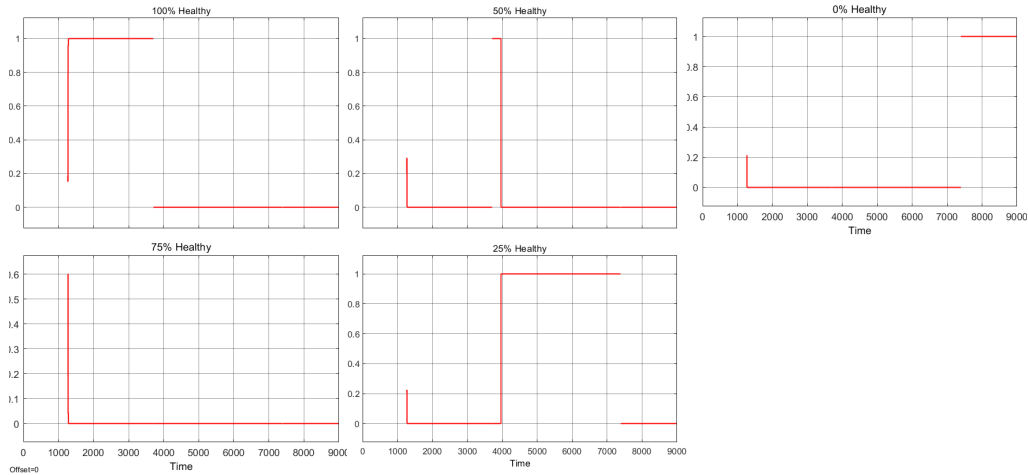


Figure 6.40: Probabilities of the five KF with two sequential faults

6.6.5 Joint State Estimation

The last FDD method tested in the multi-zone model is the Extended Kalman Filter, which is under the same scenario as the bank of Kalman Filters.

The first graph represents the EKF estimation of a , illustrated in Figure 6.41. Using the healthy calibration, see Figure 6.34, the estimated value of b is utilized as an input for the EKF to estimate a . However, since \hat{b} was too high, it results in \hat{a} (from the EKF) having an offset throughout the simulation. Although there are some inaccuracies in the calibration process, it can be concluded that the estimation remains reliable.

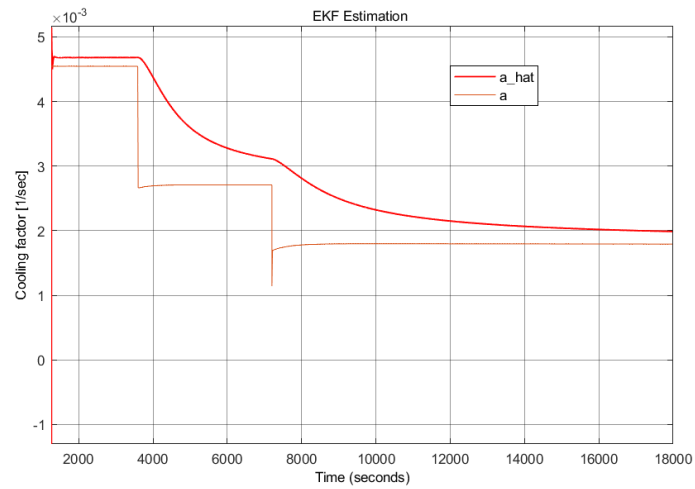


Figure 6.41: Estimation of a on the EKF with two sequential faults

Figure 6.42 illustrates how the health factor drops to 33% when the first fault occurs, and falls to 0% after the second fan breaks. This outcome suggests that both fans are coupled to each other, rather than being superimposed or combined.

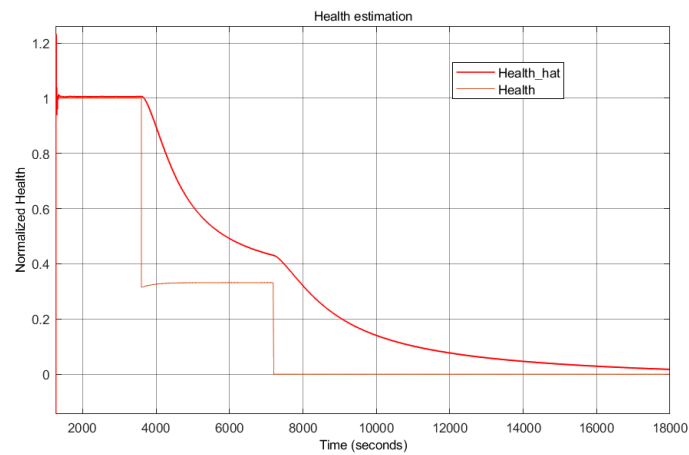


Figure 6.42: Model health estimation on the EKF with two sequential faults

Chapter 7

Discussion

This chapter will discuss the challenges and limitations faced throughout the development of the project, along with a brief description of future work.

As described in Chapter 4, some initial conditions and inputs to the system were proposed at Siemens Gamesa, which the members of the group decided to stick with throughout the project, such as constant heat generation from the electrical device, constant flow rate from both fans and considering the nacelle as the environment. Also, the single-zone model was designed without the mass balance equation and the pressures, and the air was considered incompressible. Although the single-zone limitations are covered in the multi-zone model, it would be interesting to observe the performance of the simple model with the proper thermal properties.

Determining which thermal principles to apply during the design of the multi-zone model was challenging. Various concepts were explored, such as forced ventilation or the overall heat transfer coefficient, which ultimately proved to be incorrect or unreliable, before arriving at the final result. For future work, including the nacelle dynamics holds the potential to significantly improve the robustness and give a better understanding of its interactions with the other components and the impact on the system's performance.

For this project, the calibration of the "healthy" system was conducted online, immediately followed by the initialization of the FDD algorithms. The "faulty" calibration of the system (with fans turned off) was also conducted online but in a separate run prior to the FDD tests. However, in a real scenario, both calibrations can be conducted offline prior to the FDD initialization. The calibrations require that some dynamics are introduced into the system, however, in a real scenario it will not be necessary to turn the transformer off and back on each time a new calibration is initialized, as dynamics can also be introduced by turning the fans on and off. The calibrations can instead be conducted while the system is running normally. Here the fans will need to be turned off causing the cabinet temperature to rise and data can be collected for the "faulty" calibration. The fans can then be turned back on, introducing more dynamics, and data

can be collected for the "healthy" calibration. This process can be repeated multiple times to ensure that a sufficient amount of data points have been collected for each calibration. Each calibration can then be conducted offline by simulating the collected data sequentially for the corresponding scenario.

Regarding the FDDs, a challenge with the bank of observers is associated with the gain matrix, which had to be tuned in order to improve the tracking performance of the estimated nacelle temperature. However, this tuning process resulted in increased sensitivity to measurement noise, posing a trade-off with accuracy.

In order to improve the parameter estimation, it would be appealing to combine the available EKF with the maximum likelihood technique to give an estimate that would maximize the likelihood function.

An extension to this work would also be to test how the FDDs react to other inputs to the model such as size, mass, flow rates, and heat generated by the transformer.

Since the fault detection approach in this project relied on temperature observation, the volume flow rate was manipulated, where an abrupt increase in temperature was considered equivalent to the presence of a fault in the fan. Therefore, another potential methodology for fault detection could involve monitoring the velocity of the fans and analyzing how it affects the temperature variations if the fan-curve is available. This could potentially be achieved by implementing a "cheap" encoder into the cooling fans to measure the velocity in real time.

Additional future work would be to test the available FDD algorithms on data from a real setup and, if successful, implement it into a SCADA or CMS system for fault-tolerant control (FTC).

Chapter 8

Conclusions

The task statement of this project is to detect a fault in a cooling fan by analyzing the temperature inside a control cabinet through different FDD algorithms.

To achieve this, the first task in hand was to develop a simple dynamic model that mimics the behavior of a cabinet within a nacelle. Basic thermodynamic principles were applied in order to cover the proposed suggestions by Siemens Gamesa. An extended version was created to expand the single-zone into a multi-zone model, where further thermodynamic principles were added. The simulation for both models showed satisfactory results in calculating the cabinet temperature, given the absence of real data for comparison.

Following the single-zone model, a calibration technique was then developed to identify the system parameters based on the two temperature measurements. Through trial and error, the calibration has shown reliable results for the single-zone model; for the multi-zone, the calibration resulted in an offset due to small variations in the parameters over time. A forgetting factor was introduced, however, this caused the algorithm to forget the data containing the dynamics, thus new dynamics will need to be introduced to the system. However, the RLS-based calibration without a forgetting factor was still able to estimate the system parameters within an acceptable range.

The first developed FDD method was a bank of observers where each observer assumes different scenarios regarding the "health" of the system. The residuals of each observer were generated and then normalized for comparison. The normalized residuals for the cabinet temperature were evaluated to determine which observer was the closest representation of the real system. The bank of observers was able to estimate within what range, the health status of the cabinet was located for both models. However, when there are only small differences between two residuals, the normalized values become noisy.

An MMAE method consisting of multiple Kalman filters for residual generation was also developed. Each residual and error covariance was evaluated through the likelihood function, and normalized probabilities were calculated for each Kalman filter.

The probabilities were able to show which KF had the best chance of being the correct representation of the cabinet system.

For the Joint State method, although the calibration of the multi-zone model showed some inaccuracies in parameter estimation, the algorithm was able to estimate the health within a range from the true value, making the FDD results reliable within some margin of error. Furthermore, when the estimated health is above 1, which theoretically should not occur, it gives an idea of the magnitude of the estimation error.

Finally, the task statement was completed by successfully detecting faults on a cooling fan by analyzing the control cabinet temperature through different FDD algorithms.

Bibliography

- [1] Joyce Lee and Feng Zhao. *Global Wind Report 2021*. English. Mar. 2021. URL: <https://gwec.net/wp-content/uploads/2021/03/GWEC-Global-Wind-Report-2021.pdf> (visited on 02/05/2023).
- [2] IEA. *World Energy Outlook 2022*. English. 2022. URL: <https://iea.blob.core.windows.net/assets/830fe099-5530-48f2-a7c1-11f35d510983/WorldEnergyOutlook2022.pdf> (visited on 02/05/2023).
- [3] BP. *BP Energy Outlook 2023*. English. 2023. URL: <https://www.bp.com/content/dam/bp/business-sites/en/global/corporate/pdfs/energy-economics/energy-outlook/bp-energy-outlook-2023.pdf> (visited on 02/05/2023).
- [4] Xian Wang et al. 'Analysis of long-term temperature monitoring of multiple wind turbines'. English. In: 54 (June 2021), p. 002029402110130. DOI: 10.1177/00202940211013061. URL: <https://journals.sagepub.com/doi/pdf/10.1177/00202940211013061> (visited on 07/05/2023).
- [5] Ayse Kavaz and Burak Barutcu. 'Fault Detection of Wind Turbine Sensors Using Artificial Neural Networks'. English. In: 2018 (Dec. 2018), p. 11. DOI: 10.1155/2018/5628429. URL: <https://www.hindawi.com/journals/js/2018/5628429/> (visited on 07/05/2023).
- [6] S Faulstich, B Hahn and P.J. Tavner. 'Wind turbine downtime and its importance for offshore deployment'. English. In: 14.3 (Apr. 2021), pp. 327–337. DOI: <https://doi.org/10.1002/we.421>. URL: <https://onlinelibrary.wiley.com/doi/abs/10.1002/we.421> (visited on 03/04/2023).
- [7] 'Life Cycle Reliability and Maintenance Analyses of Wind Turbines'. In: 110 (). ISSN: 1876-6102. URL: <https://www.sciencedirect.com/science/article/pii/S1876610217301789>.
- [8] Andrew Kusiak and Wenyan Li. 'The prediction and diagnosis of wind turbine faults'. English. In: 3.1 (2011), pp. 16–23. ISSN: 0960-1481. DOI: <https://doi.org/10.1016/j.renene.2010.05.014>. URL: <https://www.sciencedirect.com/science/article/pii/S0960148110002338> (visited on 07/05/2023).

- [9] 'Condition monitoring and fault detection in wind turbines based on cointegration analysis of SCADA data'. In: 116 (). ISSN: 0960-1481. URL: <https://www.sciencedirect.com/science/article/pii/S0960148117305931>.
- [10] M Blanke et al. 'Introduction to diagnosis and fault-tolerant control'. English. In: *Diagnosis and Fault-Tolerant Control*. 2nd ed. Springer, 2006, p. 15. ISBN: 978-3-540-35652-3. (Visited on 07/05/2023).
- [11] Nic Sharpley. *Nacelles*. English. Apr. 2015. URL: <https://www.windpowerengineering.com/how-is-a-nacelle-manufactured/> (visited on 09/05/2023).
- [12] Zhenyu Yang et al. 'On the single-zone modeling for optimal climate control of a real-sized livestock stable system'. English. In: Changchun, China: IEEE, 2009, pp. 3849–3854. DOI: 10.1109/ICMA.2009.5244909. URL: <https://ieeexplore.ieee.org/document/5244909> (visited on 15/05/2023).
- [13] Zhenyu Yang and Andrea Valente. 'Optimal control of offshore indoor climate'. English. In: Yokohama, Japan: IEEE, 2010, pp. 652–657. DOI: 10.1109/CCA.2010.5611080. URL: <https://ieeexplore.ieee.org/document/5611080> (visited on 15/05/2023).
- [14] Zhenyu Yang, Simon Pedersen and Petar Durdevic. 'Control of variable-speed pressurization fan for an offshore HVAC system'. English. In: Tianjin, China: IEEE, 2014, pp. 458–463. DOI: 10.1109/ICMA.2014.6885741. URL: <https://ieeexplore.ieee.org/document/6885741> (visited on 15/05/2023).
- [15] W.J.N. Turner, A. Staino and B. Basu. 'Residential HVAC fault detection using a system identification approach'. English. In: 151 (2017), pp. 1–17. ISSN: 0378-7788. DOI: <https://doi.org/10.1016/j.enbuild.2017.06.008>. URL: <https://www.sciencedirect.com/science/article/pii/S0378778816316590> (visited on 17/05/2023).
- [16] Lijun L.V. et al. 'State Detection of Switch Cabinet Based on Multi-sensor Information Fusion'. English. In: New Orleans, LA, USA: IEEE, 2019, pp. 1–6. DOI: 10.1109/FUZZ-IEEE.2019.8858925. URL: <https://ieeexplore.ieee.org/document/8858925> (visited on 17/05/2023).
- [17] Jacob Damkjær, Ubaid Bashir and Spyridon Lazaris. 'Fault Detection for Electrical Control Cabinet Temperature Management'. English. PhD thesis. Esbjerg: AAU, Dec. 2021. (Visited on 21/03/2023).
- [18] Fredrik Fogh Sørensen et al. 'Estimation of prepressure in hydraulic piston accumulators for industrial wind turbines using multi-model adaptive estimation: ASME/BATH 2019 Symposium on Fluid Power and Motion Control'. In: *Proceedings of the ASME/BATH 2019 Symposium on Fluid Power and Motion Control* (Dec. 2019). Publisher: American Society of Mechanical Engineers. DOI: 10.1115/FPMC2019-1665. URL: <https://event.asme.org/FPMC/Program/Conference-Agenda> (visited on 29/05/2023).

- [19] Zhen Sun and Zhenyu Yang. 'Application of joint parameter identification and state estimation to a fault-tolerant robot system'. English. In: Melbourne, VIC, Australia: IEEE, 2011, pp. 498–503. DOI: 10.1109/IECON.2011.6119361. URL: <https://ieeexplore.ieee.org/document/6119361> (visited on 22/05/2023).
- [20] Components RS. *Transformer*. English. 2023. URL: <https://dk.rs-online.com/web/p/chassismonterede-transformere/7387950> (visited on 22/05/2023).
- [21] Pfannenbergl. *Cooling Fans*. English. 2023. URL: <https://www.pfannenbergl.com/en/thermal-management/filterfans/filterfans/pf-65000-s1/> (visited on 22/05/2023).
- [22] Bahman Zohuri. 'Chapter 5 - First Law of Thermodynamics'. English. In: *Physics of Cryogenics*. Elsevier, 2018, pp. 119–163. ISBN: 978-0-12-814519-7. URL: <https://www.sciencedirect.com/science/article/pii/B9780128145197000057> (visited on 10/05/2023).
- [23] ROHM. *Basics of Thermal Resistance and Heat Dissipation*. English. 2016. URL: https://fscdn.rohm.com/en/products/databook/applinote/common/basics_of_thermal_resistance_and_heat_dissipation_an-e.pdf (visited on 22/05/2023).
- [24] Engineering Toolbox. *Overall heat transfer coefficients*. English. 2003. URL: https://www.engineeringtoolbox.com/overall-heat-transfer-coefficient-d_434.html (visited on 09/05/2023).
- [25] Karl Terpager Andersen. 'Theory for natural ventilation by thermal buoyancy in one zone with uniform temperature'. English. In: 38.11 (2003), pp. 1281–1289. ISSN: 0360-1323. DOI: [https://doi.org/10.1016/S0360-1323\(03\)00132-X](https://doi.org/10.1016/S0360-1323(03)00132-X). URL: <https://www.sciencedirect.com/science/article/pii/S036013230300132X> (visited on 17/05/2023).
- [26] Moncef Krarti. 'Chapter 6 - Integrated Design and Retrofit of Buildings'. English. In: *Optimal Design and Retrofit of Energy Efficient Buildings, Communities, and Urban Centers*. Butterworth-Heinemann, 2018, pp. 313–384. ISBN: 978-0-12-849869-9. URL: <https://www.sciencedirect.com/science/article/pii/B9780128498699000065> (visited on 13/05/2013).
- [27] P Heiselberg. 'Design Principles for Natural and Hybrid Ventilation'. English. In: *Aalborg University*. Indoor Environmental Engineering 2.113 (2000), p. 12. ISSN: 1395-7953. URL: https://vbn.aau.dk/ws/portalfiles/portal/197438185/Design_Principles_for_Natural_and_Hybrid_Ventilation.pdf (visited on 13/05/2023).
- [28] Nicolas Heijmans. *Impact of the Uncertainties on Wind Pressures on the Prediction of Thermal Comfort Performances*. English. Feb. 2002. URL: https://www.researchgate.net/publication/277018599_Impact_of_the_Uncertainties_on_Wind_Pressures_on_the_Prediction_of_Thermal_Comfort_Performances (visited on 12/05/2023).

- [29] Rong Li, Adrian Pitts and Yuguo Li. 'Buoyancy-driven natural ventilation of a room with large openings'. English. In: (2007), p. 9. URL: https://www.researchgate.net/publication/255590032_Buoyancy-driven_natural_ventilation_of_a_room_with_large_openings (visited on 13/05/2023).
- [30] Engineers Edge. *Ventilation Duck Stack Pressure*. English. 2021. URL: https://www.engineersedge.com/calculators/ventilation_duct_stack_pressure_15708.htm.
- [31] CoolVent. *Basics of Natural Ventilation*. English. 2023. URL: <http://coolvent.mit.edu/intro-to-natural-ventilation/basics-of-natural-ventilation/> (visited on 10/05/2023).
- [32] Yan-Bin Jia. 'Recursive Least Squares Estimation'. en. In: (). URL: <https://faculty.sites.iastate.edu/jia/files/inline-files/recursive-least-squares.pdf> (visited on 18/03/2023).
- [33] Liang Shan et al. 'Application of adaptive forgetting factor RLS algorithm in target tracking'. In: *2017 Chinese Automation Congress (CAC)*. Oct. 2017, pp. 1838–1843. doi: 10.1109/CAC.2017.8243067. (Visited on 11/05/2023).
- [34] W.K. Yung and K. F. Man. 'Optimal Selected Forgetting Factor for RLS Estimation'. English. In: 26 (1993), pp. 331–334. issn: 1474-6670. doi: [https://doi.org/10.1016/S1474-6670\(17\)49138-5](https://doi.org/10.1016/S1474-6670(17)49138-5). URL: <https://www.sciencedirect.com/science/article/pii/S1474667017491385> (visited on 22/05/2023).